https://doi.org/10.1016/j.ymssp.2022.109863

Laser Ultrasonic Imaging of Submillimeter Defect in A Thick Waveguide Using Entropy-polarized Bilateral Filtering and Minimum Variance Beamforming

Yi He[†a], Kai Wang[b], Lei Xu[a], Hoon Sohn[c,d] and Zhongqing Su[a,e,f*]

[a] Department of Mechanical Engineering
The Hong Kong Polytechnic University, Kowloon, Hong Kong SAR

[b] School of Aerospace Engineering
Xiamen University, Xiamen 361005, P.R. China

[c] Department of Civil and Environmental Engineering
Korea Advanced Institute of Science and Technology, Daejeon 34141, Republic of Korea

[d] Center for 3D Printing Nondestructive Testing
Korea Advanced Institute of Science and Technology, Daejeon 34141, Republic of Korea

[e] The Hong Kong Polytechnic University Shenzhen Research Institute
Shenzhen 518057, P.R. China

[f] School of Astronautics, Northwestern Polytechnical University, Xi'an, 710072, P.R. China

submitted to ***Mechanical Systems and Signal Processing***

(submitted on 25th May 2022; revised and re-submitted on 22nd Aug 2022)

[†] PhD Student.

[*] To whom correspondence should be addressed. Tel.: +852-2766-7818, Fax: +852-2365-4703;
Email: Zhongqing.Su@polyu.edu.hk (Prof. Zhongqing Su, *Ph.D.*)

Abstract

Recent quantum leap in far-field laser techniques has advanced noncontact implementation of nondestructive ultrasonic imaging, in pursuit of enhanced accessibility, detectability and practicability. Nevertheless, when laser-generated thermoelastic waves are extended to thick waveguides, they manifest fairly low signal-to-noise ratios (SNRs), along with severe wave diffusion, consequently lowering image resolution and contrast. With these motivations, a laser-ultrasonics imaging approach is developed, in conjunction with i) entropy-polarized bilateral filtering (Entropy-P-BF) for signal denoising, and ii) minimum variance (MV) beamforming for defect imaging, targeting at precise characterization of a submillimeter defect (with its characteristic dimension being smaller than the wave diffraction limit) in a thick waveguide. The entropy-polarized bilateral filtering denoises laser-induced ultrasonic wave signals via a two-dimensional convolution, the weight matrices of which are continuously updated according to local noise and uncertainty. With an elevated SNR, MV beamforming subsequently conducts an apodized beamforming to image the defect. Experimental validation is conducted by imaging a void-type defect, 0.7 mm only in its diameter, in a jet aero-engine turbine disk. Results prove that the developed approach is capable of characterizing a submillimeter defect accurately in a thick waveguide with thickness ~25 times the wavelength of laser-induced shear wave, regardless of a fairly low SNR (< 1dB).

***Keywords*:** signal denoising; defect imaging; laser ultrasonics; bilateral filtering; subwavelength defect; minimum variance beamforming.

1. Introduction

Ultrasonic imaging (UI) has demonstrated its effectiveness in material characterization [1, 2], nondestructive anomaly detection [2, 3], biomedical diagnosis [4] among many others. Prevailing UI approaches are implemented in a contact manner using contact-type transducers such as lead zirconate titanate (PZT) wafers [5], ultrasonic wedge transducers [6], polyvinylidene difluoride (PVDF) film sensors [7-11], nanocomposite-based ultrasound sensors [12-14], and optical fiber sensors [15]. Though acoustic coupling is warranted, the nature of the contact measurement narrows the application spectrum of UI, owing to the intrusion of contact-type transducers to the original integrity of inspected samples. Other limitations associated with the contact implementation of UI also include the narrowed bandwidth of transducers [16], larger-than-usual measurement error under a temperature-fluctuating condition [17], labor-intensive transducer installation and high cost of subsequent maintenance [18]. In pursuit of enhanced accessibility, detectability and practicability, the contactless generation and acquisition of ultrasonic signals, using such as air-coupled ultrasonic transducers [19], inductively coupled transducers [20], and laser vibrometers [21] have emerged, to circumvent, to a certain degree, the problems that the contact UI encounters. Contactless UI has found its superb applications in online quality inspection of products [22], defect awareness of specimens featuring complex geometries which are inaccessible to contact-type transducers [23], and signal acquisition in harsh working conditions [24], to name a few.

Amongst diverse means of contactless generation and acquisition of ultrasonic waves, the laser ultrasound (LU) has offered a new avenue towards high-resolution flaw detection, thickness gauging and material characterization [25-31]. The short acoustic wavelength of laser-generated ultrasound makes LU a powerful inspection tool for pinpointing flaws at the scale of millimeter [25, 26]. There is rich supply of studies to facilitate understanding of ultrasound generation and heat transfer during laser irradiation [32-34]. As revealed, the physical principle of nondestructive

LU generation lies in the thermal expansion [33-36]: in the thermo-elasto regime, ultrasound can be excited by instantaneous, dramatic thermal expansion when a focused laser pulse illuminates and heats the sample surface. When used to capture ultrasound waves, LU not only facilitates a contactless acquisition, but also enables a broadband sampling range of up to gigahertz or even terahertz, conducive to enhancement of acquisition accuracy. Of particular interest in LU-based signal acquisition are reflectometry [37-39] and interferometry [40, 41], both of which have adequate sensitivity to particulate displacements of the order of 10^1-10^2 picometers, and are therefore capable of perceiving LU-induced high-frequency ultrasound [42]. Representatively, Liu *et al*. [43] extracted nonlinear signal features of LU-generated elastic waves captured with a scanning laser interferometer, referred to as *Bhattacharyya Distance*, to image a crack of 10 mm in its length in an aluminum plate. Using a fast multi-point irradiation system integrated with a pulse laser head and a galvanometer, Wu *et al*. [29] developed a spatial gradient-based image processing technique for simultaneously locating multiple defects of different sizes ranging from 20 to 400 mm^2. To visualize an inner defect with an off-axis orientation in a thick waveguide (~50 mm in thickness), Stratoudaki *et al*. [26] made use of a total focusing map (TFM) approach, in conjunction with a full-matrix-capture method and an interferometer, to image multiple defects in an aluminum block including a series of drilled holes of 1.3 mm in diameter and varying depth from 5 to 12 mm, along with multiple slots with orientation varying from 0° to 60°. Not only limited to a structure with a regular geometry under the ordinary working condition, LU demonstrates its advantage when the inspection is extended to those with complex shapes serving in harsh working environment. Representatively, Chen *et al*. [23] utilized TFM to image five sites of defect, 3 mm in diameter each, in a geometrically complex sample, with two interferometers which were placed orthogonally one to the other, to acquire ultrasound signals from a curved surface. Addressing the difficulty using contact-type transducers for online inspection of kissing bonds and residual stress in a joint during friction stir welding, Lévesque *et al*. [44] combined 10^2-MHz LU and Fourier domain synthetic aperture focusing technique, to identify micro-scale cracks.

For monitoring geometrically complex structures of large dimensions, Jiang *et al*. [45] employed LU to obtain fast classification and evaluation of artificial rolling contact fatigue defect in rails.

Despite apparent advantages, when LU-based UI is extended to a thick waveguide, the thickness of which is at least ten times the LU wavelength, the prevailing approaches show compromised performance and degraded deficiency. This is due to multiple factors, including the low energy intensity of a generated laser pulse (to avoid ablation of inspected samples), the high excitation frequency beyond megahertz, and the long propagation distances of laser-triggered ultrasound waves in the waveguide thickness. As a result, the magnitude of laser-generated thermoelastic bulk waves (LTBWs) captured from a thick waveguide is usually of the order of tens of picometers only [46]. Consequently, changes in LTBW signals that are introduced by defect in the inspected samples (*e.g.,* wave echo or mode conversion) are prone to the contamination of ambient noises of the same order in magnitude [47]. In addition to the ultralow magnitude in intensity at a picometer scale, the reflectance of LTBWs also often presents a fairly low, yet location-dependent, signal-to-noise ratio (SNR) varying according to the local roughness of the sample surface [48]. Averaging signals acquired under the same measurement conditions may mitigate the signal uncertainty and accordingly enhance SNRs, which is, however, at the cost of increasing scanning time for repeating the measurement. To circumvent this problem, Xue *et al*. [49] recalled an ensemble empirical mode decomposition method to screen high-frequency noises in LU-induced longitudinal wave signals, for estimating the sizes of grains in an aluminum alloy sample. Ni *et al*. [50] suppressed the noise in LTBW signals using the spatial frequency selection, and imaged the defect with the synthetic aperture focusing technique, via which the acoustic waves of stronger magnitudes were selected to regulate the numerical aperture. Sadr *et al*. [51] developed a revamped denoising approach with wavelet transform and independent component analysis, to boost the number of independent components extracted from LU signals, showing superior performance in denoising LU signals with fluctuating SNRs.

Nevertheless, the above-mentioned denoising approaches, when used to denoise LTBW signals captured from a thick waveguide, usually show inferior performance, because the signal features of LTBWs (*e.g.,* wave echo or mode conversion) captured from a thick waveguide tend to be weak in magnitude (< 1 dB). Ordinary signal processing techniques are effective only in denoising LU signals with SNRs greater than 10 dB. In addition to the low SNRs of LTBW signals, the demand to precisely evaluate defect at the scale of submillimeter adds extra challenge and difficulty to LU-based UI. By way of illustration, the industrial standard, *Advisory Circular — Damage Tolerance for High Energy Turbine Engine Rotors* (AC) [52], stipulates that the threshold of a tolerable crack in an aero-engine turbine disk is 0.03 inch (*i.e.,* ~0.762 mm) only – a dimension at the submillimeter scale. LU techniques exploit LTBWs featuring a wavelength of 1~2 mm (given nanosecond laser pulse is used and a metal sample is considered) [43, 53], which approaches the diffraction limit of a defect with its size comparable to this threshold. Restricted by this, LU can be of inadequate accuracy and low imaging resolution, when attempted to characterize a subwavelength defect. To break through such a bottleneck and enhance detectability of LU-based UI, continued endeavors have been made, most of which use PZT-based contact-type transducers, assisted with signal processing such as time reversal [54], sparse array [55], minimum variance (MV) beamforming [56, 57], *etc.* Among these signal processing approaches, the MV beamforming proves its superiority in imaging spot-type scatterers in alloys [56-58]. However, the effectiveness of MV beamforming can decrease significantly when used to process LU signals of low SNRs [58, 59]. As a matter of that, imaging submillimeter defect in thick waveguides using noncontact LU remains a daunting task.

Motivated by the above challenges of existing LU-based UI, a fully noncontact UI approach is developed, targeting at precise characterization of a submillimeter defect in a thick waveguide. Addressing the low SNRs of LTBW signals acquired from a thick waveguide, the approach is

157 supplemented with i) a new denoising algorithm based on entropy-polarized bilateral filtering
158 (Entropy-P-BF) and ii) a defect imaging method based on MV beamforming. Experimental
159 validation is conducted by imaging a submillimeter defect, 0.7 mm only in its diameter, in a jet
160 aero-engine turbine disk.
161

162 **2. LTBWs in Thick Waveguide: *Excitation, Propagation and Acquisition***

163 The principle of the proposed noncontact LU-based UI is illustrated schematically in **Fig. 1**. In the
164 set-up, a pulsed laser beam is periodically generated to trigger LTBWs in the waveguide under
165 inspection, referred to as the *pump beam*; at the same time, another continuously generated laser
166 beam, the *probe beam*, illuminates the waveguide surface for detecting LTBWs. To avoid mutual
167 interference between the pump and probe beams on the same waveguide surface which is caused
168 by the local oscillation induced by the residual heat in the vicinity of the laser irradiated region
169 (a.k.a. the thermal noise during laser generation), the excitation and acquisition of LTBWs are
170 implemented on the upper and lower surfaces of the waveguide, respectively. The pump beam is
171 line-focused into a narrow band, to irradiate the upper surface and induce transient expansion,
172 which triggers LTBWs in the waveguide. The LTBWs interact with the defect (if any) in the
173 waveguide and waves are scattered by the defect. Consequently, the probe beam irradiates the
174 lower surface, and is interfered with the defect-scattered LTBWs, leading to the change in the
175 phase of the probe beam. The shift in electromagnetic phase of the probe beam is captured via
176 interferometry, and variation of the shift is associated with LTBW propagation in the waveguide.
177

178 In the above process, the constitutive equation that governs the LTBW propagation is defined by

179 $$\sigma_{i_s j_s} = 2\mu\varepsilon_{i_s j_s} + \lambda\varepsilon_0\delta_{i_s j_s}, \tag{1}$$

180 where $\sigma_{i_s j_s}$ ($i_s, j_s = x, y, z$) signifies the stress tensor; $\varepsilon_{i_s j_s}$ is the strain tensor ($\varepsilon_0 = \varepsilon_{xx} + \varepsilon_{yy} + \varepsilon_{zz}$);
181 λ and μ two Lamé constants. $\delta_{i_s j_s} = 1$ when $i_s = j_s$, and otherwise $\delta_{i_s j_s} = 0$. When the pump

beam irradiates the upper surface of the waveguide, the variance of temperature, ΔT, is induced, which introduces a boundary condition of thermal strain, $\varepsilon_{T,i_s j_s}$ (where z=0), as

$$\varepsilon_{T,i_s j_s} = -3B\gamma\Delta T\delta_{i_s j_s}, \tag{2}$$

where γ denotes the thermal expansion coefficient, and B the bulk modulus that is equal to $\lambda + 2\mu/3$. LTBW is governed by the motional equation as

$$\frac{\partial \sigma_{i_s j_s}}{\partial j_s} = \rho \frac{\partial^2 u_{i_s}}{\partial t^2}, \tag{3}$$

where ρ is the density of material, u_{i_s} the displacement components in Cartesian coordinate, and t the time. Substituting Eqs. (1) and (2) into (3), a partial differential equation is yielded as

$$(\lambda + \mu)\frac{\partial}{\partial i_s}\left(\frac{\partial u_{j_s}}{\partial j_s} - 3B\gamma\Delta T\delta_{j_s j_s}\right) + \mu\frac{\partial^2 u_{i_s}}{\partial i_s^2} = \rho\frac{\partial^2 u_{i_s}}{\partial t^2}. \tag{4}$$

In the absence of any external force, Eq. (4) can be solved after introducing initial conditions (namely, $u_{i_s} = \partial u_{i_s}/\partial t = 0$ and $\Delta T = 0$ (when $t \le 0$)), and the stress-free boundary condition (namely, $\sigma_{i_s z} = 0$ (when $z = 0$)).

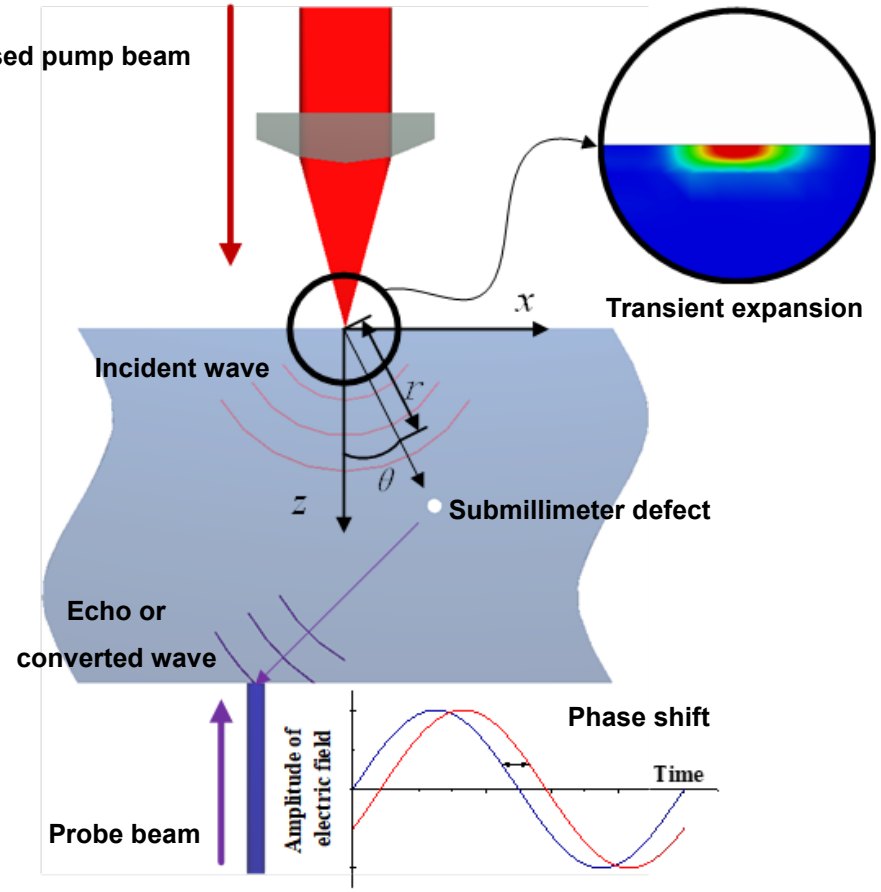

Figure 1. Schematic of the fully noncontact LU-based UI for imaging submillimeter defect in thick waveguide (2-D view).

Given a line-focused pump beam, the LTBW shows a cylindrical spreading, and therefore the polar-coordinate-form displacement field (*i.e.*, u_r and u_θ, as shown in **Fig. 1**) is adopted. By solving Eq. (4) and applying the Cartesian-to-polar conversion, the θ-related u_r and u_θ are yielded as [35]

$$u_r \propto F\left(k_L \sin\theta\right)\left(\frac{k_L \cos\theta}{\left(1-i\right)^2 k_T^2 + k_L^2 \cos^2\theta} + \frac{2ik_L^3 \sin\theta \sin 2\theta \sqrt{k_S^2 - k_L^2 \sin^2\theta}}{\left(\left(1-i\right)k_T - ik_L \cos\theta\right)\phi\left(k_L \sin\theta\right)}\right),$$
$$u_\theta \propto F\left(k_S \sin\theta\right)\frac{ik_S^4 \sin 4\theta}{\left(\left(1-i\right)k_T + \sqrt{k_S^2 \sin^2\theta - k_L^2}\right)\phi\left(k_S \sin\theta\right)}, \quad (5)$$

where

$$\begin{cases} F\left(x_\lambda\right)=\int_{-\infty}^{\infty} I\left(x\right)e^{-ix_\lambda x}\mathrm{d}x, \\ \phi\left(x_\lambda\right)=\left(2x_\lambda^2-k_S^2\right)^2-4x_\lambda^2\sqrt{\left(x_\lambda^2-k_L^2\right)\left(x_\lambda^2-k_S^2\right)} \end{cases}, \quad \left(x_\lambda = k_L\sin\theta \text{ or } k_S\sin\theta\right) \tag{6}$$
$$k_T=\sqrt{\frac{\omega C}{2a}}.$$

In Eqs. (5) and (6), $I\left(x\right)$ denotes the spatial distribution of the laser irradiation over the waveguide surface, $F\left(x_\lambda\right)$ the Fourier transform of $I\left(x\right)$, $\phi\left(x_\lambda\right)$ the Rayleigh determinant, k_L and k_S the wavenumbers of longitudinal and shear modes of LTBWs. x_λ is the projection along the *x*-axis of the wavenumber of longitudinal (for $F\left(x_\lambda\right)$) or shear (for $\phi\left(x_\lambda\right)$) mode of LTBWs, ω the central frequency of LTBW, C the specific heat capacity, a the thermal conductivity, and i the imaginary unit. It is noted in Eq. (5) that the generated LTBW field manifests specific directivity that gives rise to an angle-dependent magnitude of the displacement field. As a result of this, blind zones may exist during defect detection, in which LTBW is of a low intensity and therefore weakly interacts with the defect.

Considering the directivity of LTBWs in a thick waveguide, the low intensity of incident longitudinal LTBW, and interference of environmental noise, as well as the fact that wave excitation and acquisition are conducted on the two opposite waveguide surfaces as illustrated in **Fig. 1**, the shear-to-longitudinal (S-to-L) mode conversion is utilized in the approach. This is in part attributed to the strongest magnitude of the S-to-L mode of LTBW among all the echo and conversion modes generated by the defect. In addition, the significant difference in the propagation velocity between the shear and longitudinal wave modes facilitates separation of the converted longitudinal wave from the incident shear wave, benefiting subsequent signal processing and interpretation.

3. Denoising and Imaging Algorithm

Envisaging the fairly low SNRs of LTBW signals scattered by a submillimeter defect in a thick waveguide, a denoising algorithm based on entropy-polarized bilateral filtering (BF) (Section 3.1) and a defect imaging method based on minimum variance (MV) beamforming (Section 3.2) are developed.

3.1 Entropy-based Bilateral Filtering

3.1.1 Signal Pre-arrangement

Raw LTBW signals, which are captured at different signal acquisition points on the waveguide surface under the same laser irradiation condition (*i.e.,* the same laser irradiation position and laser intensity), are first pre-arranged in a three-dimensional (3-D) domain, in which the *x*-axis represents acquisition points in sequence, *y*-axis the time and *z*-axis the signal amplitude, in **Fig. 2 (a)**. The top view of the 3-D presentation is referred to as the *signal sequence images* (SSIs) hereinafter. The spectrum of a representative raw LTBW signal is presented in **Fig. 2 (a)**, to observe that the key signal components distribute within a range from 0.5 to 4 MHz. **Figures 2 (b)-(d)** show the SSIs obtained after averaging 200, 100, and 50 raw LTBW signals which are acquired under the identical laser irradiation condition, indicating that averaging raw LTBW signals can facilitate recognition of signal features, but at a limited degree.

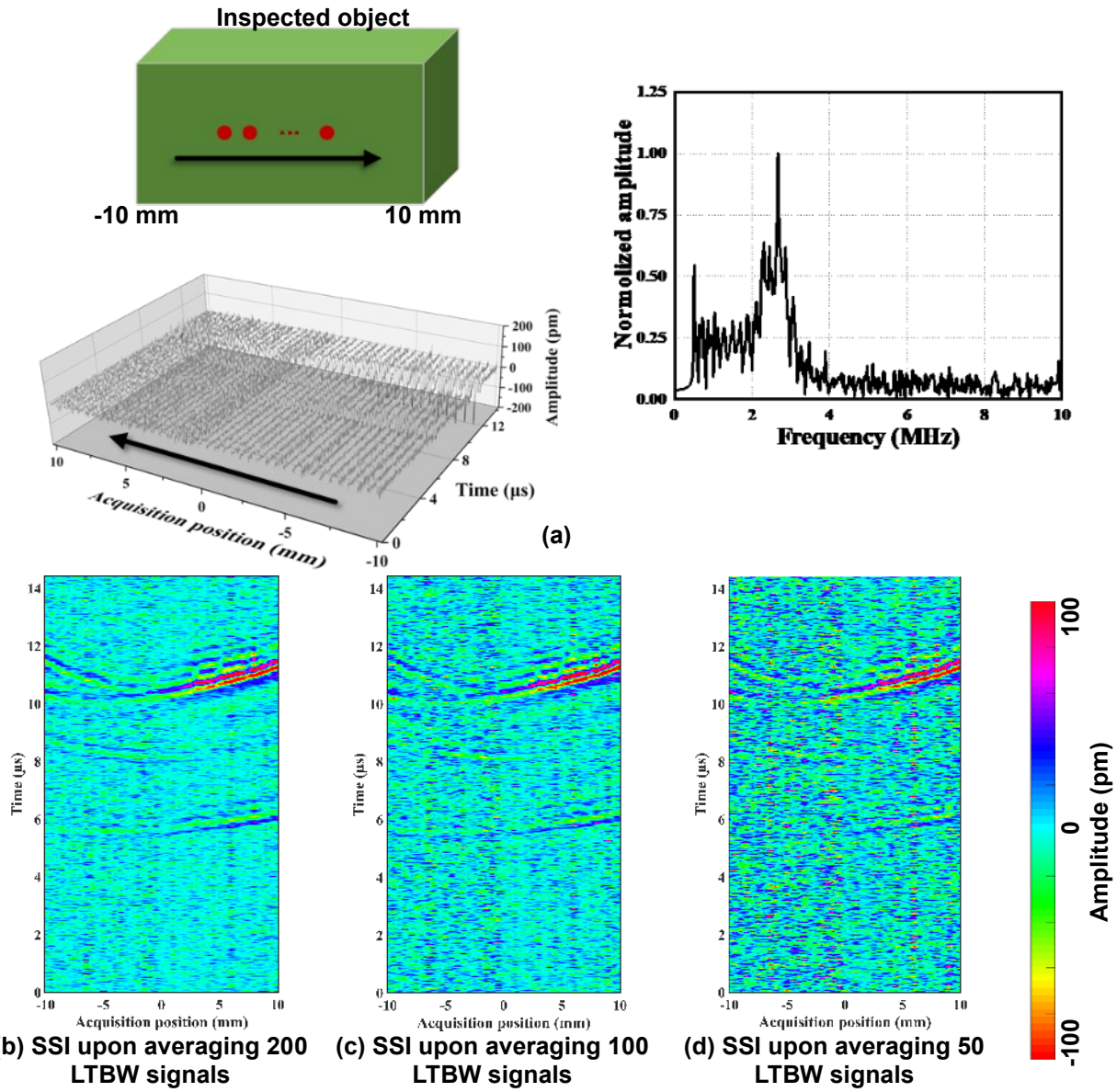

Figure 2. (a): LTBW signals pre-arranged in the order of acquisition points (red points), to produce an SSI, and frequency spectrum of a representative raw LTBW signal; (b)-(d): SSIs obtained upon averaging 200, 100 and 50 LTBW signals, under the same laser irradation condition

3.1.2 Bilateral Filter (BF)

BF is a denoising algorithm to rapidly execute pixel-wise denoising of a gray or a chromatic digital image. BF originates from the conventional Gaussian filter – a classical linear smoothing filter that reconstructs the image value at each pixel by weighted-averaging its adjacent pixels according to a 2-D Gaussian distribution function, and this function is referred to as *kernel*. Different from the

conventional Gaussian filter, BF updates the kernel by scalar-multiplying the original kernel of the Gaussian filter (which is termed the *spatial kernel* in BF) and a *range kernel* (which quantifies the difference in values between the pixel to-be-denoised and its adjacent pixels).

Consider an arbitrarily selected pixel of an SSI, $p_{i_0 j_0}$, as indicated in **Fig. 3 (a)**. $p_{i_0 j_0}$ is centralized in a segment of the SSI, $\boldsymbol{X}_{i_0 j_0}$, and it locates at the i_0-th row ($i_0 = 1, \cdots, L_{T,SSI}$, where $L_{T,SSI}$ denotes the number of pixels along *y*-axis of an SSI) and the j_0-th column ($j_0 = 1, \cdots, L_{S,SSI}$, where $L_{S,SSI}$ is the number of pixels along *x*-axis of an SSI). Specifically in this approach, the spatial kernel of BF is a spatial-temporal kernel $\boldsymbol{K}_{ST}$, which, together with the range kernel $\boldsymbol{K}_{V,i_0 j_0}$ (note that the matrices $\boldsymbol{K}_{ST}$, $\boldsymbol{K}_{V,i_0 j_0}$ and $\boldsymbol{X}_{i_0 j_0}$ are of the same dimension) can be calculated via [60] (**Fig. 3 (b)**)

$$
\begin{aligned}
k_{ST}(k,l) &= \frac{1}{2\pi\sigma_S\sigma_T}\exp\left(-\frac{\left(k-\left(L_T+1\right)/2\right)^2}{2\sigma_T^2}-\frac{\left(l-\left(L_S+1\right)/2\right)^2}{2\sigma_S^2}\right), \\
k_{V,i_0 j_0}(k,l) &= \frac{1}{\sqrt{2\pi}\sigma_V}\exp\left(-\frac{\left(X_{i_0 j_0}(k,l)-p_{i_0 j_0}\right)^2}{2\sigma_V^2}\right),
\end{aligned}
\tag{7}
$$

where $k_{ST}(k,l)$, $k_{V,i_0 j_0}(k,l)$ and $X_{i_0 j_0}(k,l)$ signify individual elements of $\boldsymbol{K}_{ST}$, $\boldsymbol{K}_{V,i_0 j_0}$ and $\boldsymbol{X}_{i_0 j_0}$ in the *k*-th row ($k = 1, \cdots, L_T$, where L_T denotes the number of pixels along *y*-axis of $\boldsymbol{X}_{i_0 j_0}$) and the *l*-th column ($l = 1, \cdots, L_S$, where L_S represents the number of pixels along *x*-axis of $\boldsymbol{X}_{i_0 j_0}$), respectively. σ_S and σ_T are the standard deviations of the 2-D Gaussian distribution that the individual elements of $\boldsymbol{K}_{ST}$ follow, while σ_V is the standard deviation of the one-dimensional Gaussian distribution that the individual elements of $\boldsymbol{K}_{V,i_0 j_0}$ follow. Note that $\boldsymbol{K}_{ST}$ is independent of $p_{i_0 j_0}$, whereas $\boldsymbol{K}_{V,i_0 j_0}$ is $p_{i_0 j_0}$-dependent. Equation (7) indicates that $k_{ST}(k,l)$ decreases as the distance between $X_{i_0 j_0}(k,l)$ and $p_{i_0 j_0}$ increases; and $k_{V,i_0 j_0}(k,l)$ decreases as the difference in values between $X_{i_0 j_0}(k,l)$ and $p_{i_0 j_0}$ increases. With Eq. (7), the kernel of BF, $\boldsymbol{K}_{i_0 j_0}$, can be

obtained by (**Figs. 3 (b) and (c)**)

$$\boldsymbol{K}_{i_0 j_0} = \boldsymbol{K}_{ST} \cdot \boldsymbol{K}_{V,i_0 j_0}, \tag{8}$$

where the operator "$\cdot$" represents the scalar multiplication, which denotes that each element of $\boldsymbol{K}_{i_0 j_0}$ in the k-th row and the l-th column is produced by multiplying $k_{ST}(k,l)$ of $\boldsymbol{K}_{ST}$ and the corresponding $k_{V,i_0 j_0}(k,l)$ of $\boldsymbol{K}_{V,i_0 j_0}$. With Eq. (8), the pixel value $p_{i_0 j_0}$ is re-defined as

$$p_{i_0 j_0 - R} = \frac{\boldsymbol{e}^{\mathrm{T}} \left(\boldsymbol{X}_{i_0 j_0} \cdot \boldsymbol{K}_{i_0 j_0} \right) \boldsymbol{e}}{\boldsymbol{e}^{\mathrm{T}} \boldsymbol{K}_{i_0 j_0} \boldsymbol{e}}, \tag{9}$$

where $p_{i_0 j_0 - R}$ is the re-defined pixel and $\boldsymbol{e}$ a column vector with all its elements being one. Superscript "T" represents the transpose operation of matrix.

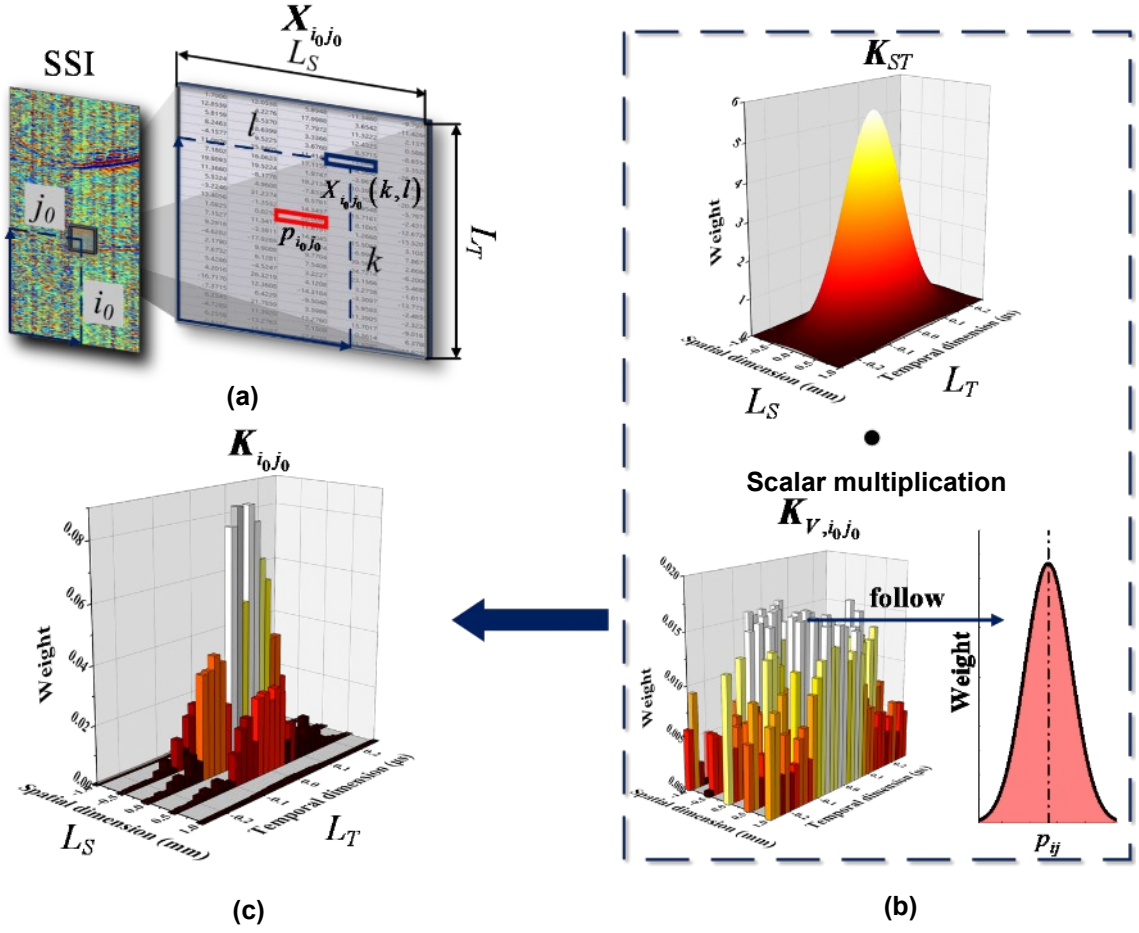

Figure 3. Procedure of generating the kernel of BF: (a) a segment of SSI, at center of which pixel $p_{i_0 j_0}$ locates; (b) the spatial-temporal kernel $\boldsymbol{K}_{ST}$ and range kernel $\boldsymbol{K}_{V,i_0 j_0}$; (c) kernel $\boldsymbol{K}_{i_0 j_0}$ for $\boldsymbol{X}_{i_0 j_0}$ obtained by Eq. (8).

With the 2-D convolution operation, Eqs. (7), (8) and (9) are executed throughout the entire SSI.

BF possesses the capability of *edge-preserving* (EP) for an image, and in another word the range kernel in BF tends to retain pixel values that are singular from the rest in the image, such as the image edges or damage-induced singularity. That is because BF can maintain the high-frequency components of SSIs – those represented by the key image features (*e.g.*, image edges or damage-induced singularity). For illustration, **Figs. 4 (a)-(d)** show a noise-polluted SSI, along with images processed with BF and Gaussian filter, respectively. Comparison implies that BF preserves more sharpness of the image and loses less high-frequency signal information, than the Gaussian filter does. The capability of EP that BF possesses ensures that a denoised SSI will not be over-averaged as the Gaussian filter usually does. A consequence of the over-averaging is a blurred image with reduced image resolution. In this approach, the high-frequency components in LTBW signals (*i.e.,* those scattered in a frequency range from 0.5 to 4 MHz) substantially define the image resolution and contrast.

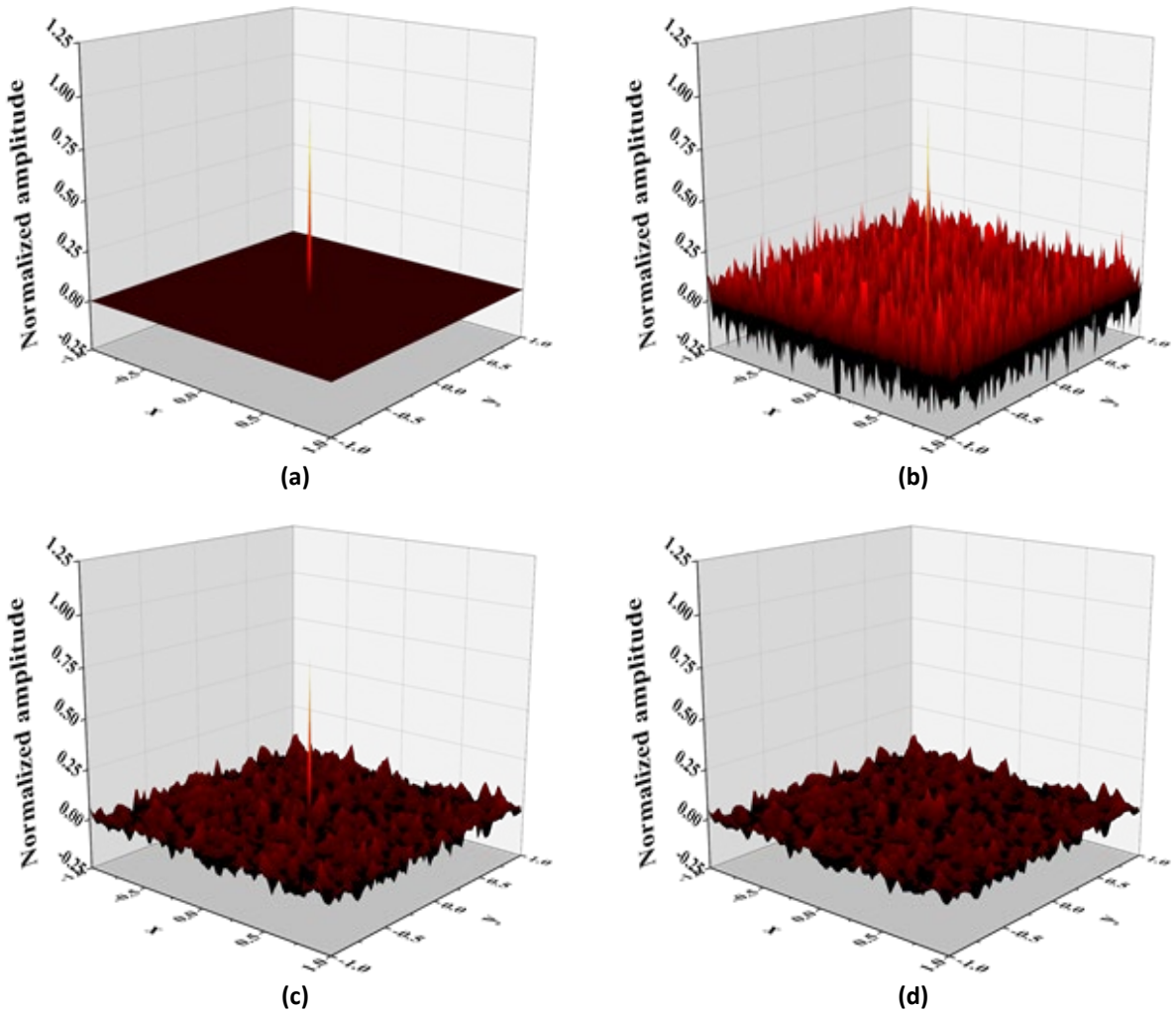

311 **Figure 4.** Comparison between BF- and Gaussian-filter-based image denoising: (a) a noise-free SSI containing
312 a narrowed pulse centralized in SSI; (b) white-noised-added image of (a); (c) BF-denoised image of (b); (d)
313 Gaussian-filter-denoised image of (b).
314

315 ### 3.1.3 Polarized Bilateral Filter (P-BF)

316 Equations (7)-(9) applies BF-based denoising on an SSI with the same intensity of EP on the two
317 orthogonal dimensions - temporal and spatial dimensions, because the range kernel of BF entails
318 the same Gaussian distribution function on the two dimensions simultaneously. It is, however,
319 envisaged that in practical implementation, the intensity of EP, on different dimensions, is
320 preferably selected independently one from the other, so as to entertain distinct resolutions of the
321 SSI in the temporal and spatial dimensions.
322

To this end, the P-BF proposed in this study allows independent intensity of EP on the temporal and spatial dimensions. The polarization of BF enables different types of Gaussian distribution, uniform distribution, or mix of both, to be applied on different rows of the range kernel ($\boldsymbol{K}_{PBF-V,i_0j_0}$). As shown in **Fig. 5 (a)**, i) for the central row of $\boldsymbol{K}_{PBF-V,i_0j_0}$, *i.e.,* the ($(L_T+1)/2$)-th row, the Gaussian distribution is applied, as defined in Eq. (7); ii) for the rest of the rows of $\boldsymbol{K}_{PBF-V,i_0j_0}$, a threshold b is defined first. Provided that the distance between a specific row and the central row (*i.e.,* $\left|k-(L_T+1)/2\right|$) is less than b , this row is named the *adjacent row*, or otherwise the *distant row*. For an adjacent row, the distribution of its individual elements follows

$$GU\left(x_{ran},p_{i_0j_0},k\right)=c_{Guassian}\frac{1}{\sqrt{2\pi}\sigma_V}e^{-\frac{\left(x_{ran}-p_{i_0j_0}\right)^2}{2\sigma_V^2}}+c_{uniform}\frac{1}{6\sigma_V},$$
$$\text{where } \left|k-\frac{\left(L_T+1\right)}{2}\right|<b,\ c_{uniform}=\frac{\left|k-\frac{\left(L_T+1\right)}{2}\right|}{b},\ c_{Guassian}=1-c_{uniform}, \tag{10}$$

where $GU\left(x_{ran},p_{i_0j_0},k\right)$ denotes Gaussian-uniform-mixed distribution which is the sum of a Gaussian distribution and a uniform distribution of the element, dependent on both $p_{i_0j_0}$ and k ; x_{ran} is a variable, to be replaced with $X_{i_0j_0}\left(k,l\right)$ when Eq. (10) is calculated; $c_{Guassian}$ and $c_{uniform}$ are the scale factors of Gaussian distribution and uniform distribution, respectively. Equation (10) implies that for a given adjacent row that is the k -th row of $\boldsymbol{K}_{PBF-V,i_0j_0}$, $c_{Guassian}$ and $c_{uniform}$ are linearly assigned by k , on which basis the integration of $GU\left(x_{ran},p_{i_0j_0},k\right)$ with respect to x_{ran} is equal to one. It is noted that the longer the distance between an adjacent row to the central row the larger $c_{uniform}$ it will be, and the closer it approaches one. Once $c_{uniform}=1$ and consequently $c_{Guassian}=0$, $GU\left(x_{ran},p_{i_0j_0},k\right)$ is converted to a uniform distribution $U\left(x_{ran}\right)$ as

$$U\left(x_{ran}\right)=\frac{1}{6\sigma_V}. \tag{11}$$

342 It is specified that individual elements of a distant row follow the distribution of $U\left(x_{ran}\right)$, in which

343 x_{ran} is to be replaced with individual elements of distant rows. Substituting $\boldsymbol{X}_{i_0 j_0}$ into Eqs. (10)

344 and (11) as the variables, $\boldsymbol{K}_{PBF-V,i_0 j_0}$ can be calculated via

345
$$k_{PBF-V,i_0 j_0}\left(k,l\right)=\begin{cases} GU\left(X_{i_0 j_0}\left(k,l\right),p_{i_0 j_0},k\right), & \left|k-\dfrac{\left(L_T+1\right)}{2}\right|<b \\ \dfrac{1}{6\sigma_V}, & \left|k-\dfrac{\left(L_T+1\right)}{2}\right|\geq b \end{cases} \tag{12}$$

346 where $k_{PBF-V,i_0 j_0}\left(k,l\right)$ signifies the element of the *k*-th row and *l*-th column of $\boldsymbol{K}_{PBF-V,i_0 j_0}$. With the

347 above modified range kernel, there are $L_T-\left(2b+1\right)$ elements in each column of $\boldsymbol{K}_{PBF-V,i_0 j_0}$ which

348 are equal to $1/\left(6\sigma_V\right)$, regardless of the location and value of $p_{i_0 j_0}$.

349

350 In this way, P-BF acts as a quasi-Gaussian filter on the temporal dimension. Note that a

351 conventional Gaussian filter, *per se*, does not conduct EP, while the quasi-Gaussian-filter, as

352 defined by Eq. (10), weakens EP on the temporal dimension. In the meantime, on the spatial

353 dimension of the SSI, the elements of the central and adjacent rows of $\boldsymbol{K}_{PBF-V,i_0 j_0}$ follow a regular

354 Gaussian distribution and $GU\left(x_{ran},p_{i_0 j_0},k\right)$ performs the normal EP. Similar to $\boldsymbol{K}_{i_0 j_0}$, the kernel

355 of P-BF, $\boldsymbol{K}_{PBF,i_0 j_0}$ (**Fig. 5 (b)**), can be obtained by scalar multiplication between $\boldsymbol{K}_{ST}$ and

356 $\boldsymbol{K}_{PBF-V,i_0 j_0}$ as

357
$$\boldsymbol{K}_{PBF,i_0 j_0}=\boldsymbol{K}_{ST}\cdot\boldsymbol{K}_{PBF-V,i_0 j_0}. \tag{13}$$

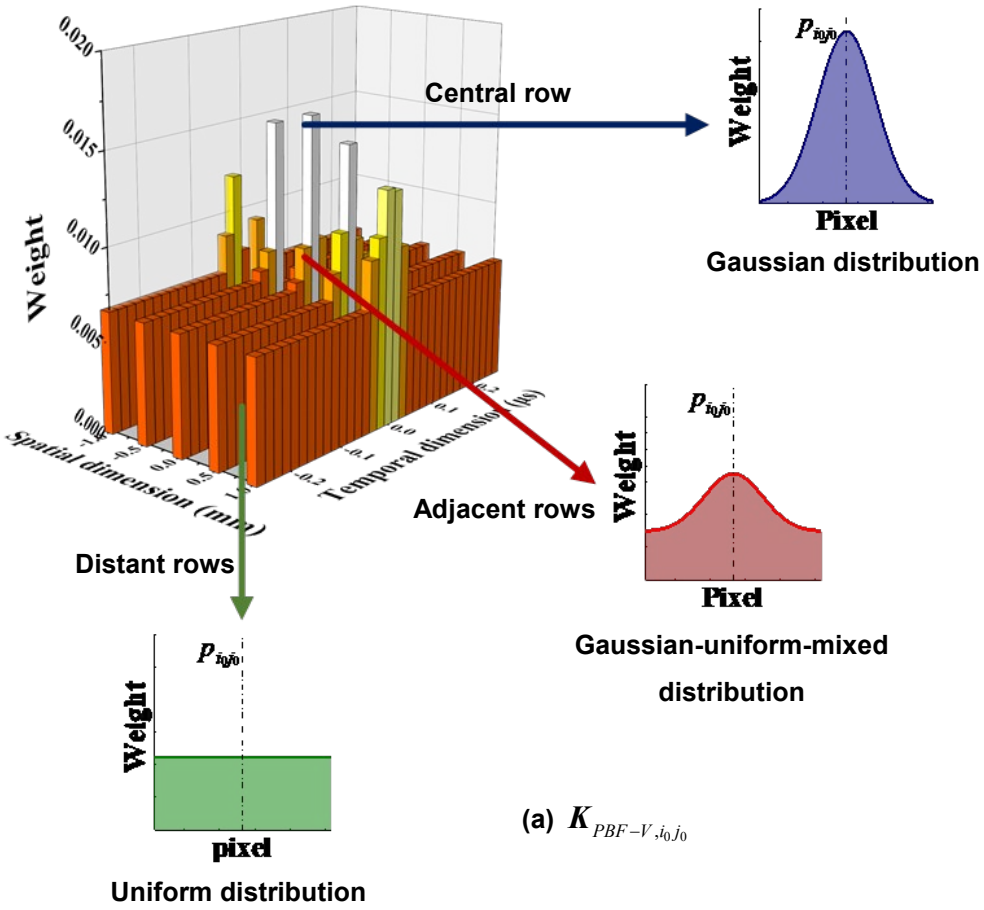

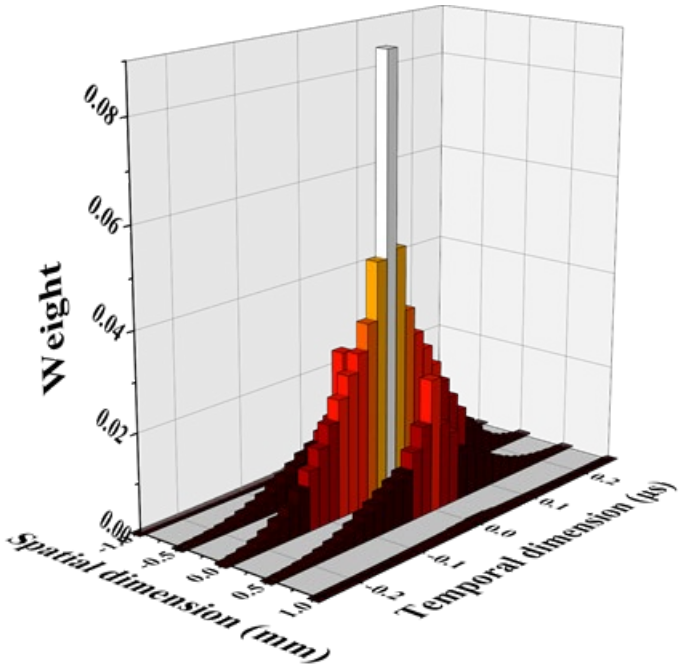

Figure 5. Procedure of generating the kernel of P-BF: (a) the range kernel of P-BF determined by different distributions (blue: Gaussian distribution; green: uniform distribution; red: Gaussian-uniform-mixed distribution); (b) kernel of P- BF obtained by Eq. (13).

The P-BF allows different intensities to be applied on the temporal and spatial dimensions that are independent one to the other. It is such a trait of P-BF that satisfies the need of denoising at different resolutions on two dimensions of an SSI. With P-BF, the columns of SSI, *i.e.,* the LTBW signals are denoised, and the rows of SSI, which characterize the location of signal acquisition points, remain the original sharpness of peaks and valleys.

3.1.4 Adaptive Estimate of Local Signal Uncertainty: *Entropy-based BF*

P-BF implements independent EP on the temporal and spatial dimensions of an SSI with different distributions that are followed by the elements of adjacent and distant rows of $\boldsymbol{K}_{PBF-V,i_0j_0}$, respectively. Nevertheless, the P-BF lies in a hypothesis that SNR on the spatial dimension remains constant, in Eqs. (7), (8), (9), and (12). However, the defect-converted wave mode manifests itself as an instantaneous pulse in an SSI, due to the broadband nature of the probe beam, and consequently the SNR of a LTBW signal varies on the temporal dimension: local SNRs increase in the presence of defect-induced mode conversion, and *vice versa*. Ignorance of such variation can result in distorted denoising, because the hypothesis of a constant SNR in P-BF leads to a constant EP on the temporal dimension, which is insufficient to preserve the sharpness of the peaks of an SSI and accordingly over-flats the pulse peaks.

To circumvent this deficiency of P-BF, adaptive estimate of local SNRs is introduced to supplement P-BF in this study. The local SNRs are the measure of the correlation between the determinacy and uncertainty in a noise-polluted signal [61, 62]. The determinacy indicates a pure signal component, yet uncertainty characterizes the noise. To quantify uncertainty, the information entropy (IE), referred to as *Shannon entropy*, is introduced, serving as a criterion to regulate the range kernel of P-BF.

Continue using $p_{i_0j_0}$ — an arbitrary pixel of an SSI, for illustration. To obtain IE of $p_{i_0j_0}$, a column

vector $\boldsymbol{x}_{i_0j_0}$, with N elements ($N \le L_T$; N is an odd), is extracted from the central column of $\boldsymbol{X}_{i_0j_0}$. The pixel $p_{i_0j_0}$ is the middle element of $\boldsymbol{x}_{i_0j_0}$. For an arbitrarily selected element of $\boldsymbol{x}_{i_0j_0}$, the following two probabilities exist:

$$\begin{aligned} P\left(\boldsymbol{x}_{i_0j_0} < 0\right) &= \frac{n_{\boldsymbol{x}_{i_0j_0}<0}}{N}, \\ P\left(\boldsymbol{x}_{i_0j_0} \ge 0\right) &= \frac{n_{\boldsymbol{x}_{i_0j_0}\ge 0}}{N}, \end{aligned} \tag{14}$$

where $n_{\boldsymbol{x}_{i_0j_0}<0}$ and $n_{\boldsymbol{x}_{i_0j_0}\ge 0}$ denote the numbers of elements in $\boldsymbol{x}_{i_0j_0}$, the value of which are less than and greater than/equal to 0, respectively. With that, the IE of $p_{i_0j_0}$, $E\left(p_{i_0j_0}\right)$ (unit: Bit), is calculated via [62]

$$E\left(p_{i_0j_0}\right) = -\left[P\left(\boldsymbol{x}_{i_0j_0} < 0\right)\log_2\left(P\left(\boldsymbol{x}_{i_0j_0} < 0\right)\right) + P\left(\boldsymbol{x}_{i_0j_0} \ge 0\right)\log_2\left(P\left(\boldsymbol{x}_{i_0j_0} \ge 0\right)\right)\right]. \tag{15}$$

As both $P\left(\boldsymbol{x}_{i_0j_0} < 0\right)$ and $P\left(\boldsymbol{x}_{i_0j_0} \ge 0\right)$ fall in a range from zero to one, it is noted in Eq. (15) that $E\left(p_{i_0j_0}\right)$ is non-negative. In particular, when $E\left(p_{i_0j_0}\right) = 0$, it mathematically indicates that $\boldsymbol{x}_{i_0j_0}$, corresponding to $p_{i_0j_0}$, is fully deterministic (with no noise).

Applying Eq. (15) on Eq. (12), the range kernel of Entropy-P-BF, $\boldsymbol{K}_{EPBF-V,i_0j_0}$, is then defined as

$$k_{EPBF-V,i_0j_0}\left(k,l\right) = \begin{cases} GU\left(X_{i_0j_0}\left(k,l\right), p_{i_0j_0}, k\right), & \text{when } \left|k - \dfrac{\left(L_T+1\right)}{2}\right| < b\left(E\left(p_{i_0j_0}\right)\right) \\ \dfrac{1}{6\sigma_V}, & \text{when } \left|k - \dfrac{\left(L_T+1\right)}{2}\right| \ge b\left(E\left(p_{i_0j_0}\right)\right) \end{cases} \tag{16a}$$

$$b\left(E\left(p_{i_0j_0}\right)\right) = \begin{cases} f_s T_{S-LTBW}/4, & \text{when } E\left(p_{i_0j_0}\right) = 0 \\ f_s T_{S-LTBW}/8, & \text{when } E\left(p_{i_0j_0}\right) \ge 0 \end{cases} \tag{16b}$$

where $k_{EPBF-V,i_0j_0}\left(k,l\right)$ signifies the element of the k-th row and l-th column of $\boldsymbol{K}_{EPBF-V,i_0j_0}$. f_s is the sampling rate, and T_{S-LTBW} the period of the shear mode of LTBW. Equation (16b) re-defines

b in P-BF as a binarized function subject to $E\left(p_{i_0 j_0}\right)$. With $b\left(E\left(p_{i_0 j_0}\right)\right)$, the boundary between the adjacent and distant rows can now be adaptively determined by $E\left(p_{i_0 j_0}\right)$ in Entropy-P-BF, which endows the Entropy-based BF with the capability of processing SSI with various local SNRs. Same as $\boldsymbol{K}_{i_0 j_0}$ and $\boldsymbol{K}_{PBF,i_0 j_0}$, the kernel of Entropy-P-BF, $\boldsymbol{K}_{EPBF,i_0 j_0}$, can be obtained by scalar multiplication, as

$$\boldsymbol{K}_{EPBF,i_0 j_0} = \boldsymbol{K}_{ST} \cdot \boldsymbol{K}_{EPBF-V,i_0 j_0}. \tag{17}$$

Equations (16) and (17) define the Entropy-P-BF in this approach.

Figure 6 illuminates the denoising process of an SSI using Entropy-P-BF. An IE map is first obtained for the SSI, with Eq. (15). For a pixel, at which $E\left(p_{i_0 j_0}\right)=0$ (*e.g.,* the peak of a pulse), $p_{i_0 j_0}$ is fully deterministic, and Eq. (16) implies that those rows in $\boldsymbol{K}_{PBF-V,i_0 j_0}$, the distance of which to the central row of $\boldsymbol{K}_{PBF-V,i_0 j_0}$ is no more than $f_s T_{S-LTBW}/4$, are the adjacent rows. Under this circumstance the P-BF approaches BF, and EP on the temporal dimension preserves high-frequency components of LTBW signals (greater than 0.5 MHz in this case) – key image features including peaks of all the pulses. In the contrast, when $E\left(p_{i_0 j_0}\right)>0$ at a specific pixel, Eq. (16) applies $f_s T_{S-LTBW}/8$ to *b*, and the P-BF retreats to the quasi-Gaussian filter. Consequently, the EP on the temporal dimension suppresses high-frequency components of LTBW signals, and in the meantime mitigates background noise.

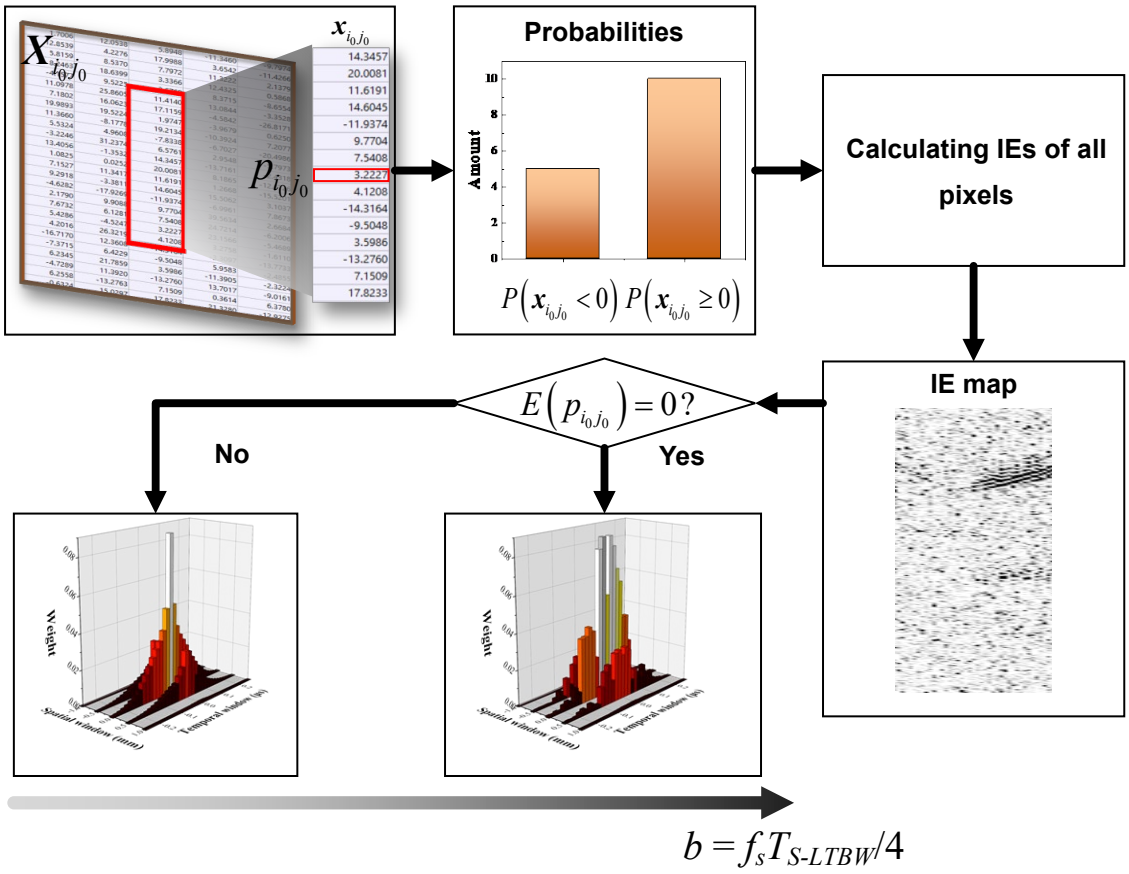

Figure 6. Flowchart of SSI denoising using Entropy-P-BF.

3.2 Minimum Variance (MV) Beamforming

With the Entropy-P-BF, SSIs are denoised and SNRs of LTBW signals are enhanced. The enhanced LTBW signals are subsequently used to image defect with the MV beamforming. MV beamforming narrows the Full-Width-at-Half-Maximum (FWHM) of an image and boosts the image contrast. Here, FWHM is defined as the width between two pixels of an image, field values of which are equal to half of the peak field value of the image. FWHM is a key feature that calibrates the resolution of an image. MV beamforming, sharing the same principle with that of the delay-and-sum (DAS) beamforming, applies different degrees of time delay to a batch of LTBW signals, so as all the LTBW signals arrive at an acquisition point at the same time. The traveling time of a wave mode in LTBW signal (*i.e.*, the S-to-L mode, in this study. In principle, various wave modes can be used for MV beamforming [63], while the S-to-L mode in LU signals is utilized as interpreted in Section 2.) is the time that the wave mode takes to travel from the laser

437 irradiation point to the defect, and then from the defect, upon mode conversion, to the signal
438 acquisition point. The delay is determined according to the length of the irradiation-defect-
439 acquisition path and the phase velocities of the shear and longitudinal wave modes. Upon delay, a
440 DAS image can be created, in which the pixel value is equal to the magnitude of an aligned LTBW
441 signal. Repeating the above operation to all the aligned LTBW signals creates a series of DAS
442 images.
443
444 Consider the j_0-th column of a denoised SSI, $\boldsymbol{S}_{j_0}$, which is a denoised LTBW signal that is obtained
445 when the laser irradiation is at $\left(x_{j_0,ir}, z_{j_0,ir}\right)$ and acquisition at $\left(x_{j_0,acq}, z_{j_0,acq}\right)$, as shown in **Fig. 7**
446 **(a)**. With $\boldsymbol{S}_{j_0}$, a DAS image, $\boldsymbol{D}_{j_0}$, is created via

$$\boldsymbol{D}_{j_0}\left(i_1, j_1\right) = \boldsymbol{S}_{j_0}\left(t_{j_0,(i_1,j_1)}/t_s\right),$$
447 $$\text{where } t_{j_0,(i_1,j_1)} = \frac{\sqrt{\left(x_{(i_1,j_1)} - x_{j_0,ir}\right)^2 + \left(z_{(i_1,j_1)} - z_{j_0,ir}\right)^2}}{v_{S-LTBW}} + \frac{\sqrt{\left(x_{(i_1,j_1)} - x_{j_0,acq}\right)^2 + \left(z_{(i_1,j_1)} - z_{j_0,acq}\right)^2}}{v_{L-LTBW}}, \quad (18)$$

448 where, $\boldsymbol{D}_{j_0}\left(i_1, j_1\right)$ represents the pixel located at the i_1-th row and the j_1-th column of $\boldsymbol{D}_{j_0}$ (here,
449 $i_1 = 1, \cdots, L_x$, and $j_1 = 1, \cdots, L_z$. L_x and L_z denote the numbers of pixels along x- and z-axes in $\boldsymbol{D}_{j_0}$,
450 respectively.). $x_{(i_1,j_1)}$ and $z_{(i_1,j_1)}$ are the x- and z-coordinates of the pixel $\boldsymbol{D}_{j_0}\left(i_1, j_1\right)$, respectively.
451 v_{S-LTBW} and v_{L-LTBW} are the phase velocities of the shear and longitudinal wave modes of LTBW,
452 respectively. t_s is the time interval for signal acquisition. $\boldsymbol{S}_{j_0}\left(t_{(i_1,j_1)}/t_s\right)$ is the $t_{j_0,(i_1,j_1)}/t_s$ -th
453 element of $\boldsymbol{S}_{j_0}$. Equation (18) is applied to $\boldsymbol{S}_{j_0}$, to obtain its DAS image. Averaging all DAS
454 images results in a raw DAS image, $\boldsymbol{D}$, as

$$\boldsymbol{D} = \frac{\sum_{j_0=1}^{L_{S,SSI}} \boldsymbol{D}_{j_0}}{L_{S,SSI}}. \quad (19)$$
455

456 The dimension of each $\boldsymbol{D}_{j_0}$ is identical to that of $\boldsymbol{D}$. The peak in the $\boldsymbol{D}$ denotes the presence of

defect.

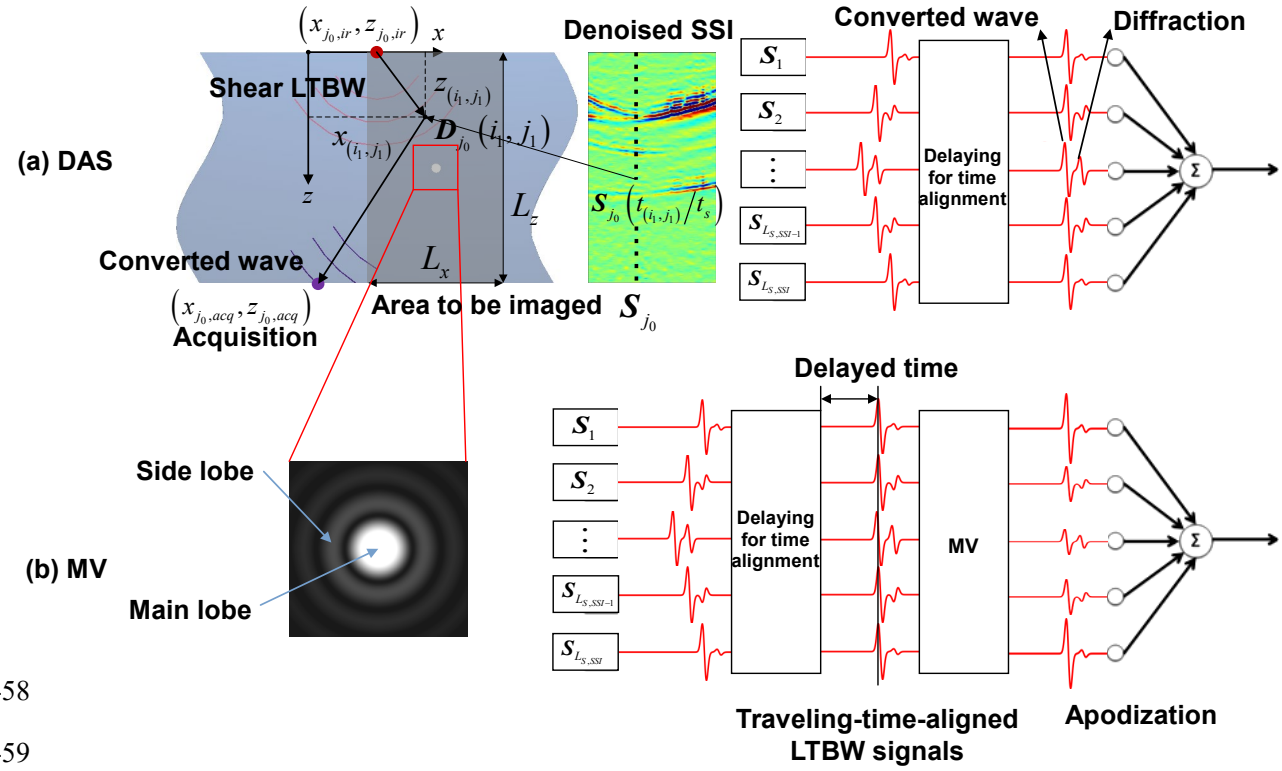

Figure 7. (a) The principle of DAS beamforming; (b) the principle of MV beamforming.

Notwithstanding, given that the dimension of a submillimeter defect is less than the diffraction limit of the LTBW, wave diffraction cannot be safely negligible, and hence DAS-based beamforming can become untenable without considering the wave diffraction, as illustrated in **Fig. 7 (a)**. The diffraction limit, D_{diff}, is defined as [64]

$$D_{diff} \approx 0.61\lambda_{S-LTBW} \cdot \frac{\sqrt{d_{defect-acq}^2 + \left(D_{acq}/2\right)^2}}{D_{acq}/2}, \tag{20}$$

where λ_{S-LTBW} is the wavelength of the shear mode of LTBW, $d_{defect-acq}$ the distance from the defect to the sample surface on which LU signals are acquired, and D_{acq} the distance between the first and the last acquisition points on the sample surface. The diffraction is responsible for the emergence of side lobes in a DAS image, as seen in **Fig. 7 (b)**, which are undesirable patterns to elongate the FWHM of the image, leading to artifacts in a DAS image.

To suppress the side lobes, the MV beamforming [57] conducts apodization following Eq. (18), as illustrated in **Fig. 7 (b)**. For each pixel, the value is the sum of the magnitudes of all the aligned LTBW signals that are weighted via apodization. Here, the apodization indicates the searching for a series of weight coefficients, $w_{i_1 j_1, j_0}$, so as to minimize each pixel of $\boldsymbol{D}$ out of the main lobe [65]

$$\boldsymbol{D}_{MV}\left(i_1, j_1\right) = \sum_{j_0=1}^{L_{S,SSI}} w_{i_1 j_1, j_0} \boldsymbol{D}_{j_0}\left(i_1, j_1\right), \quad \text{where} \sum_{j_0=1}^{L_{S,SSI}} w_{i_1 j_1, j_0} = 1 \tag{21}$$

where $\boldsymbol{D}_{MV}$ denotes the MV-regulated $\boldsymbol{D}$, and $\boldsymbol{D}_{MV}\left(i_1, j_1\right)$ is the pixel located at the i_1-th row and the j_1-th column of $\boldsymbol{D}_{MV}$. Mathematically, the MV beamforming minimizes $\left|\boldsymbol{D}_{MV}\left(i_1, j_1\right)\right|$ by regulating $w_{i_1 j_1, j_0}$ under the constrain of unity that the sum of $w_{i_1 j_1, j_0}$ is equal to one (*i.e.*, $\sum_{j_0=1}^{L_{S,SSI}} w_{i_1 j_1, j_0} = 1$). Here, the minimization of $\left|\boldsymbol{D}_{MV}\left(i_1, j_1\right)\right|$ is implemented by minimizing $\boldsymbol{D}_{MV}^2\left(i_1, j_1\right)$ instead of $\left|\boldsymbol{D}_{MV}\left(i_1, j_1\right)\right|$ itself, to mathematically facilitate the minimization. $\boldsymbol{D}_{MV}^2\left(i_1, j_1\right)$ is first vectorized as

$$\begin{aligned} &\boldsymbol{D}_{MV}^2\left(i_1, j_1\right) = \boldsymbol{w}_{i_1 j_1}^{\mathrm{T}} \boldsymbol{R}_{i_1 j_1} \boldsymbol{w}_{i_1 j_1}, \\ &\text{where } \boldsymbol{R}_{i_1 j_1} = \left[\boldsymbol{D}_1\left(i_1, j_1\right) \quad \cdots \quad \boldsymbol{D}_{L_{S,SSI}}\left(i_1, j_1\right)\right]^{\mathrm{T}} \left[\boldsymbol{D}_1\left(i_1, j_1\right) \quad \cdots \quad \boldsymbol{D}_{L_{S,SSI}}\left(i_1, j_1\right)\right], \text{ and} \\ &\boldsymbol{w}_{i_1 j_1} = \left[w_{i_1 j_1, 1} \quad \cdots \quad w_{i_1 j_1, L_{S,SSI}}\right]^{\mathrm{T}}. \end{aligned} \tag{22}$$

In the above $\boldsymbol{R}_{i_1 j_1}$ is the cross-spectral density matrix. With the constrain of $\sum_{j_0=1}^{L_{S,SSI}} w_{i_1 j_1, j_0} = 1$, it has

$$\min_{\boldsymbol{w}_{i_1 j_1}} \boldsymbol{w}_{i_1 j_1}^{\mathrm{T}} \boldsymbol{R}_{i_1 j_1} \boldsymbol{w}_{i_1 j_1}, \text{ subject to } \sum_{j_0=1}^{L_{S,SSI}} w_{i_1 j_1, j_0} = 1, \tag{23}$$

where the operation of $\min_{\boldsymbol{w}_{i_1 j_1}} \boldsymbol{w}_{i_1 j_1}^{\mathrm{T}} \boldsymbol{R}_{i_1 j_1} \boldsymbol{w}_{i_1 j_1}$ regulates $\boldsymbol{w}_{i_1 j_1}$, so as to minimize $\boldsymbol{w}_{i_1 j_1}^{\mathrm{T}} \boldsymbol{R}_{i_1 j_1} \boldsymbol{w}_{i_1 j_1}$. For a point-like defect, an ameliorated version of $\boldsymbol{R}_{i_1 j_1}$, $\hat{\boldsymbol{R}}_{i_1 j_1}$, is defined as [57]

$$\hat{\boldsymbol{R}}_{i_1 j_1} = \frac{1}{2}\left(\boldsymbol{R}_{i_1 j_1} + \boldsymbol{J}\boldsymbol{R}_{i_1 j_1}^{\mathrm{T}}\boldsymbol{J} + \frac{\mathrm{Tr}\left(\boldsymbol{R}_{i_1 j_1}\right)}{L_{S,SSI}}\right), \tag{24}$$

where $\boldsymbol{J}$ is a matrix with all its antidiagonal elements are equal to 1 and the rest are 0; $\mathrm{Tr}\left(\boldsymbol{R}_{i_1 j_1}\right)$

denotes the operation extracting the trace of $\boldsymbol{R}_{i_1 j_1}$. Recalling the method of Lagrange multipliers [65, 66], and replacing $\boldsymbol{R}_{i_1 j_1}$ by $\hat{\boldsymbol{R}}_{i_1 j_1}$, $\boldsymbol{w}_{i_1 j_1}$ can be obtained as

$$\boldsymbol{w}_{i_1 j_1} = \frac{\hat{\boldsymbol{R}}_{i_1 j_1}^{-1} \boldsymbol{e}}{\boldsymbol{e}^{\mathrm{T}} \hat{\boldsymbol{R}}_{i_1 j_1}^{-1} \boldsymbol{e}}. \tag{25}$$

Substituting Eqs. (25) to (21), the MV-refined image $\boldsymbol{D}_{MV}$ is obtained, to image the defect, if any, in the waveguide.

4. Experimental Validation

To validate effectiveness of the developed LU-based UI that is facilitated by the denoising and imaging algorithm, experiment is conducted, in which a piece of an aero-engine turbine disk containing a submillimeter internal defect is imaged.

4.1 Experimental Set-up

The schematic of experimental set-up is shown in **Fig. 8**. The set-up consists of a pulsed-laser pump system, an assembly of optical lenses, a three-axis stage, and a laser Doppler vibrometer data-acquisition (LDV-DAQ) system. The pulsed-laser pump system is a compact pulsed Nd: YAG diode-pumped solid slate laser device (QUANTEL® Centurion+ 50 mJ), and it emits a pulsed laser beam with the modifiable pulse repetition frequency (PRF) variable from 1 to100 Hz, the optical wavelength of 1,064 nm, the duration of 12 ns, the irradiation area of 3.2 mm × 3.2 mm, and the energy intensity ranging from 0 to 50 mJ. The assembly of optical lenses is installed in a 60-mm coaxial cage (LUBON®), including a cylindrical lens with the 100 mm focal length (LUBON® CY107R14) and a beam expander with multiples ranging from twofold to sixfold (Daheng Optics® GCO-2505). The lens and expander are placed in sequence between the sample and the pulsed-laser pump system, as shown in **Fig. 8 (b)**. Via the beam expander, the raw pump beam is quadrupled, each measuring 12.8 mm × 12.8 mm. The cylindrical lens narrows the horizontal size

of the expanded beam to 0.8 mm× 12.8 mm. The pump beam, captured with an infrared camera, **Fig. 8 (c)**, is invisible. The three-axis stage horizontally displaces the sample along the *x*-axis to receive the laser irradiation. The LDV-DAQ (Polytec® PSV-500) measures LTBW responses with a visible laser beam of the optical wavelength of 633 nm and the intensity less than 1 mW, toggles the detection positions, and registers the data. All instruments and the sample are immobilized on an optical platform, immune to ambient vibration.

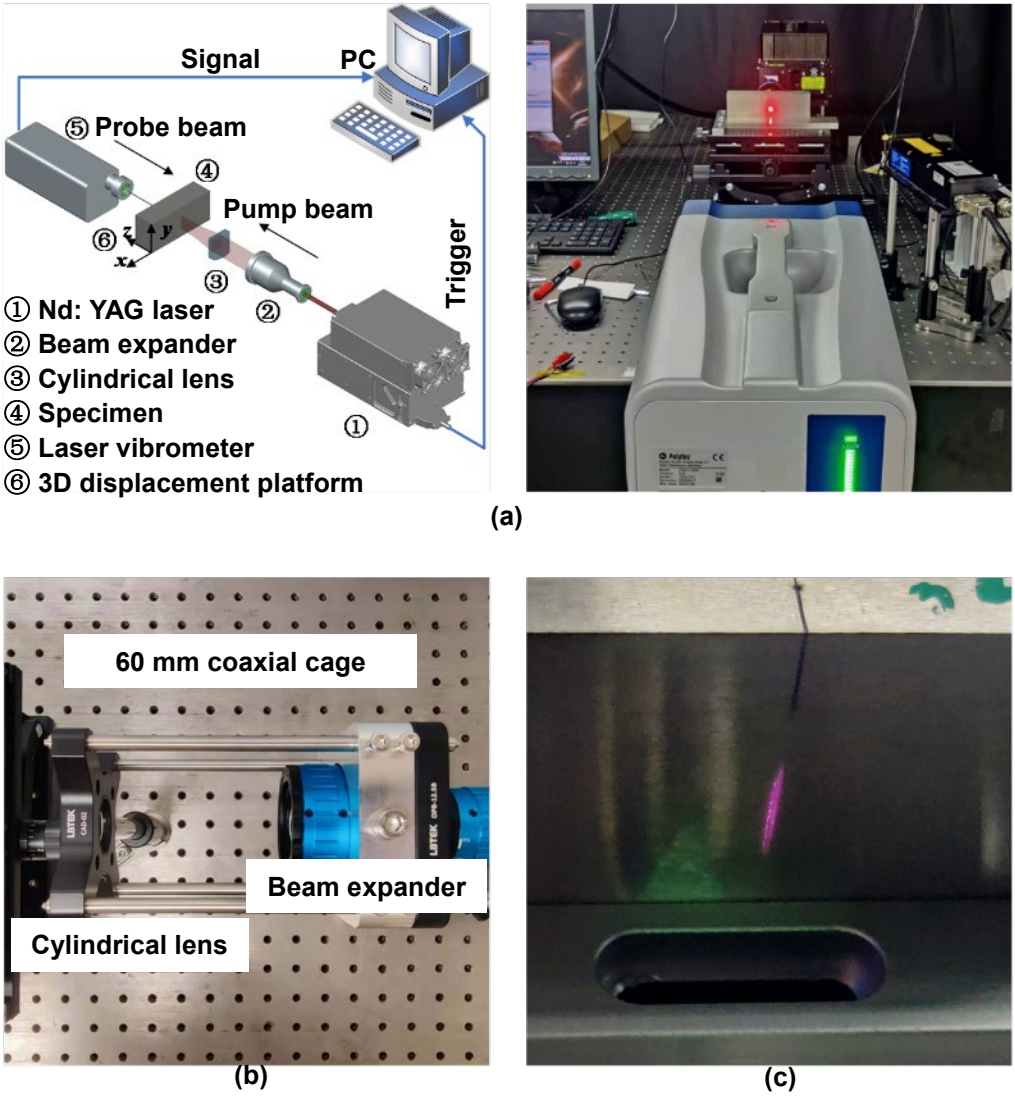

Figure 8. Experiment for implementing fully contactless LU-based UI: (a) schematic of experimental setup; (b) assembly of lenses; (c) re-shaped pump beam (0.8 mm× 12.8 mm), illuminating the sample surface.

4.2 Specimen

The sample is a piece cut from an aero-engine turbine disk – a nickel-based superalloy (FGH4096), with its key material parameters in **Tab. 1** [67]. The superalloy features the phase transition temperature of 700 K, which withstands a single-pulse energy of 15 mJ, corresponding to the laser irradiance of 11.27 MW/cm^2. The sample measures 150 mm × 30 mm × 50 mm, **Fig. 9 (a)**. The sample is pre-treated with a submillimeter defect – a through hole with its diameter being 0.7 mm, **Fig. 9 (b)**.

Table 1. Key material properties of nickel-based superalloy (FGH4096) [67].

λ	(Lamé's first parameter, GPa)	132.80
μ	(Lamé's second parameter, GPa)	86.34
ρ	(Density, g/cm^3)	8.32
γ	(Linear expansion coefficient, 10^{-6} K^{-1})	11.3
C	(Specific heat capacity, J/(kg•K))	6.6×10^{-3}
a	(Thermal conductivity, W/(m•K))	6.9
T_M	(Melting temperature, K)	1006.85
T_P	(Phase transition temperature, K)	756.85

4.3 Experimental Procedure

The line-shaped pump beam illuminates the front surface of the sample along five lines (marked as irradiating lines 1-5 in **Fig. 9 (a)**) parallel to the *y*-axis and evenly spaced with an interval of 2.5 mm. LTBWs are acquired on the back surface of the sample at up to 41 equidistant acquisition points with an interval of 0.5 mm. A retroreflective tape (**Fig. 9 (c)**) is surface-adhered on the acquisition area, to enhance the intensity of the reflected probe beam.

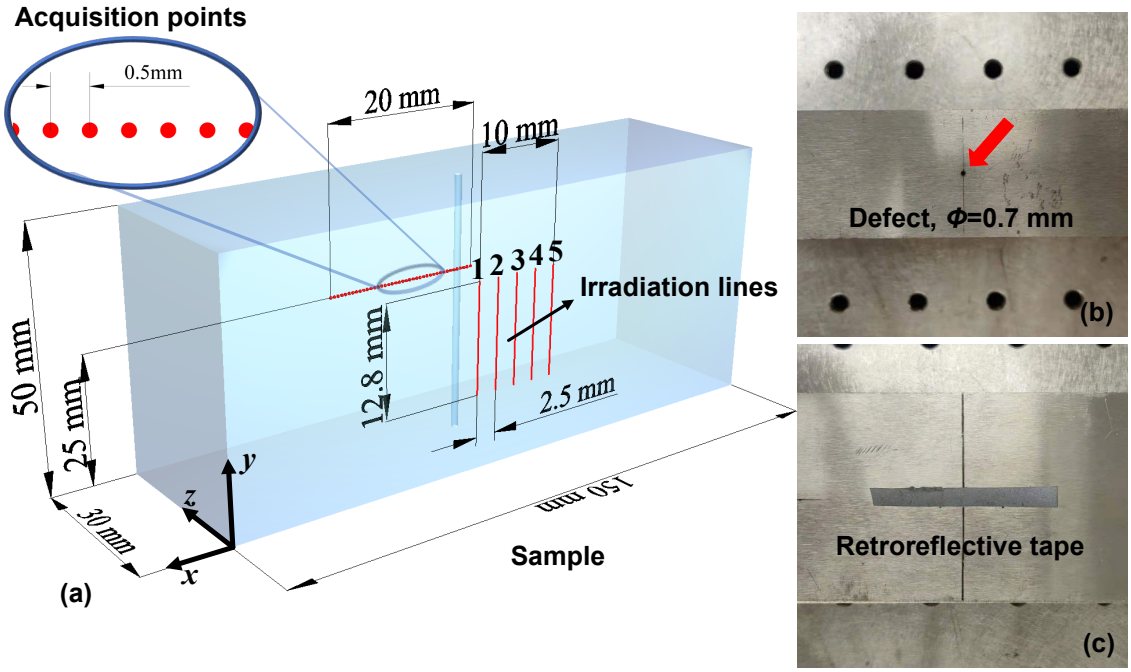

Figure 9. (a) Schematic of sample (dimensions not in real scale); (b) close-up photo of the through-hole type defect with the diameter of 0.7 mm; (c) back surface of sample, on which LTBW signals are acquired.

For each laser irradiation, the PRF is set to be 100 Hz, and the pulse energy to be 15 mJ which is below the ablation threshold of the specimen material. The pulsed-laser pump system emits a periodical pulsed laser beam, and the LDV DAQ system is synchronized to emit the probe beam. The out-of-plane displacements induced by LTBW at the sample surface are measured at the 41 acquisition points with the LDV DAQ system, at a sampling rate of 62.5 MHz. At each acquisition point, 200, 100 and 50 LTBW signals are acquired under each laser irradiation. A high-pass filter with the cut-off frequency of 500 kHz is set to screen low-frequency ambient noise.

The developed denoising and imaging algorithm is applied on the acquired LTBW signals: first, all LTBW signals are pre-arranged to create SSI (Section 3.1.1); second, the SSI is denoised with the Entropy-P-BF to elevate SNRs (Section 3.1.3); last, the defect is imaged with SNR-enhanced LTBW signals, via MV beamforming.

5. Results and Discussion

The accuracy and precision of defect imaging obtained using the Entropy-P-BF and MV beamforming is compared against those using conventional signal processing approaches.

5.1 BF *vs.* P-BF *vs.* Entropy-P-BF

Three SSIs, having different intensities of background noise, are processed using BF, P-BF and Entropy-P-BF, with results shown in **Fig. 10**. Comparison reveals that BF, P-BF and Entropy-P-BF are able to smooth background noise and highlight defect-induced mode conversion. In particular, Entropy-P-BF shows the highest SNR when compared with P-BF and BF, which exhibits the improvement of SNR in magnitude by an order, given that 50 LTBW signals are averaged. A major drawback of BF is that the peaks and valleys of the pulses are distorted, due to the same denoising resolution applied on both the temporal and spatial dimensions (therefore the same EP intensity on both dimensions). In the contrast, with different degrees of denoising resolution and EP intensity in two dimensions, P-BF and Entropy-P-BF increase the SNRs, not at the cost of distorting pulse peaks and valleys.

The refining of SSIs upon denoising is apparent in the time-frequency domain. **Figure 11** presents the spectrograms of a LTBW signal, and three counterpart signals that are pre-processed with BF, P-BF and Entropy-P-BF. Results affirm that all three denoising approaches are capable of suppressing the lower- or higher-frequency components out range of the key signal components (referring to signal spectrum in **Fig. 2 (a)**). However, Entropy-P-BF outperforms the others in preserving the key signal components in the range from 0.5 to 4 MHz. The defect images obtained with MV beamforming, using SSIs denoised by BF, P-BF, and Entropy-P-BF, are compared in **Fig. 12**. Without the denoising process, MV beamforming naturally fails imaging the defect. Compared with P-BF and BF, the Entropy-P-BF in conjunction with MV beamforming shows the best imaging performance.

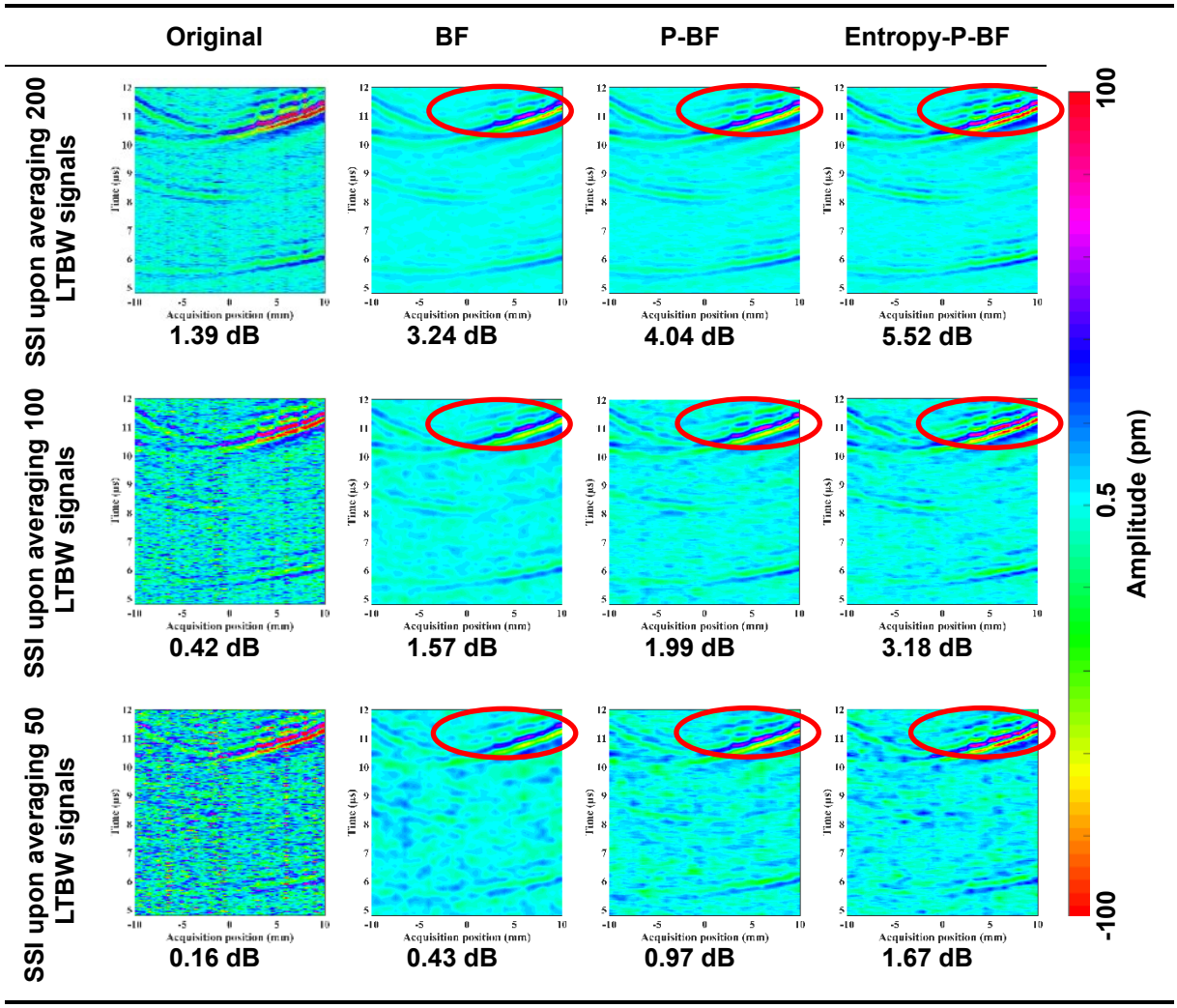

588 **Figure 10.** SSIs, upon averaging 200, 100 and 50 LTBW signals, and denoised results processed with BF, P-
589 BF, and Entropy-P-BF (red ellipses pointing out the peaks of pulses in LTBW signals that are distorted in
590 results with BF, but not in others).
591

592 In addition, the improvement of SNRs upon Entropy-P-BF is at the expense of only a slight
593 increase in computational cost. To put it into perspective, for the example signals shown in **Fig.**
594 **10**, in which each SSI features 900 × 41 pixels, the runtime of executing BF, P-BF and Entropy-
595 P-BF is 0.114 s, 0.145 s, and 0.175 s, respectively (based on a computer having a CPU with 20
596 logical processors, 3.20 GHz of clock speed and 64 GB RAM.). In practice, the dimension of an
597 SSI takes quadratic expansion with the increase of the sample surface area to be imaged, and
598 therefore the cost-effectiveness is an important merit of Entropy-P-BF.

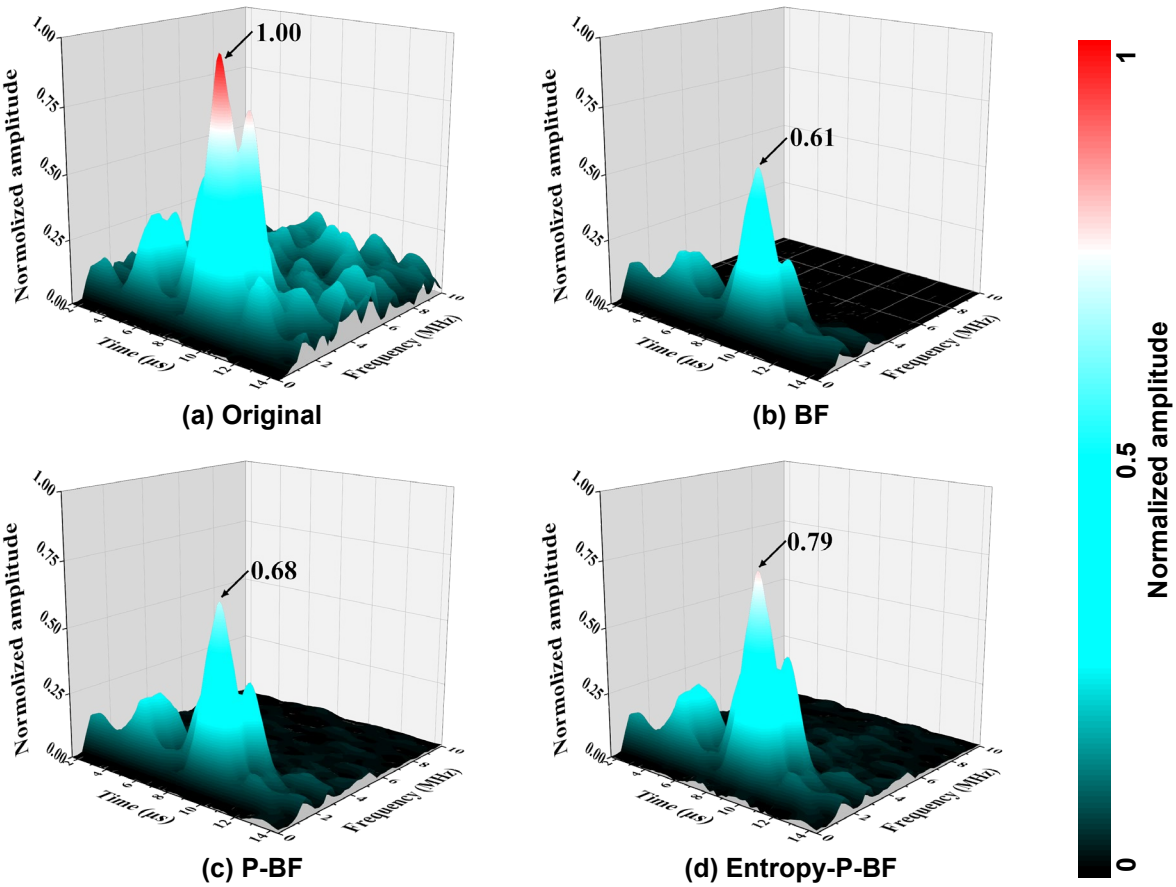

599 **Figure 11.** Spectrograms of (a) a LTBW signal segment; (b) BF-denoised, (c) P-BF-denoised, and (d) Entropy-
600 P-BF-denoised signal in (a).
601
602
603
604
605
606
607
608
609
610
611

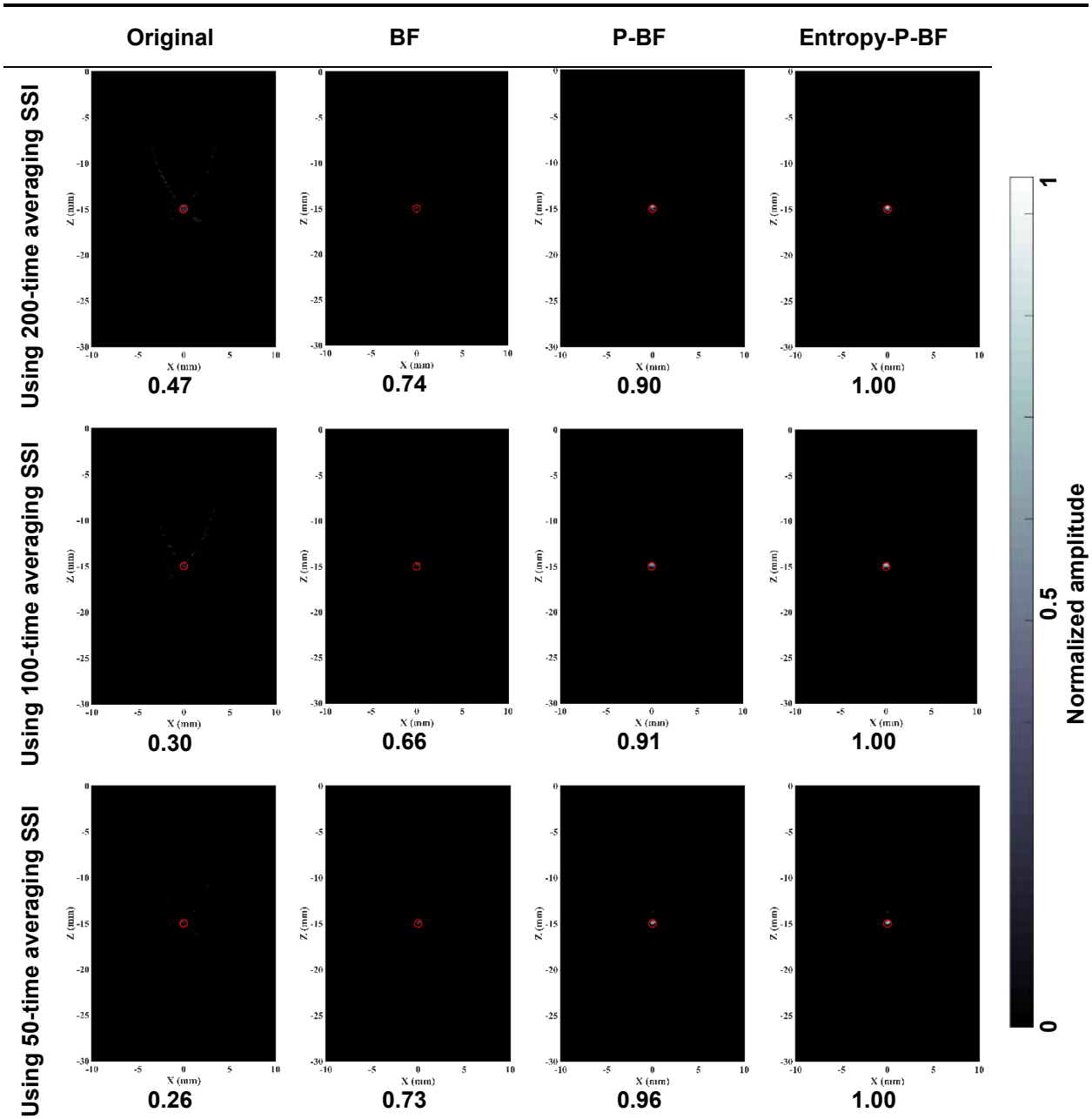

612 **Figure 12.** Defect images obtained with MV beamforming using SSIs, upon averaging 200, 100 and 50 LTBW
613 signals and denoised with BF, P-BF and Entropy-P-BF (red circle: real location and dimension of defect; value
614 below image indicating the maximum relative intensity of pixel at defect location).
615

616 ## 5.2 DAS *vs.* MV Beamforming

617 **Figure 13** compares defect images obtained with conventional DAS-based and MV beamforming-
618 based imaging algorithms, to observe plenty of side lobes in the DAS-processed image, **Fig. 13**
619 **(a)**, owing to the ignorance of the wave diffraction components in LTBW signals. With the

apodization conducted via MV beamforming, those side lobes are eliminated, **Fig. 13 (b)**. To quantitively illustrate the difference in between, two line spread functions, along two orthogonal lines crossing the defect location, are obtained and presented in **Figs. 13 (c)** and **(d)**, showing respective FWHM in two images. It is noted that FWHM reduces from 1.01 mm to 0.79 mm, and from 3.04 mm to 0.67 mm, respectively, in two dimensions of the sample, which represents an increase in image resolution by 21.78% and 74.01%, respectively. In addition, significant reduction in the number of side lobes is noted, conducive to the improvement of imaging accuracy and precision.

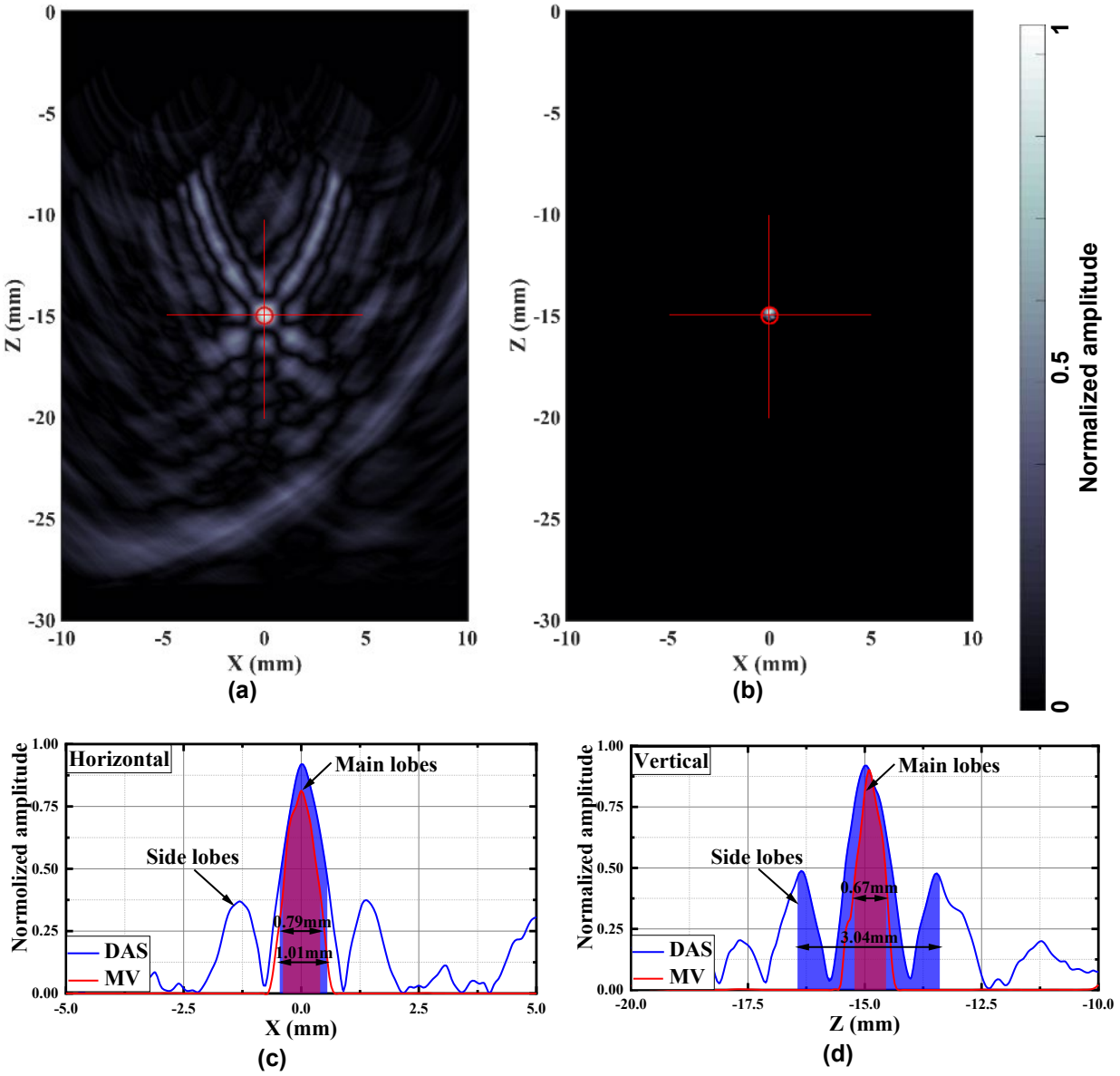

Figure 13. Defect images obtained with DAS-based and MV beamforming-based algorithms: (a) DAS; (b) MV beamforming; (c) and (d) the horizontal and line vertical spread functions near defect, respectively.

6. Concluding Remarks

Aimed at conducting contactless imaging of the submillimeter defect in a thick waveguide, a LU-based UI approach is developed, in conjunction with i) a new denoising algorithm based on entropy-P-BF and ii) a defect imaging method based on MV beamforming. The entropy-P-BF denoises laser-induced ultrasonic wave signals, to remarkably improve SNRs, and MV beamforming subsequently conducts an apodized beamforming to image the defect. The accuracy and precision of the developed LU-based UI are verified by experiment, in which a void-type defect, 0.7 mm only in its diameter, in a jet aero-engine turbine disk is imaged precisely. Results affirm that the new approach is capable of characterizing a submillimeter defect accurately in a waveguide with thickness ~25 times the wavelength of laser-induced shear wave, regardless of a fairly low SNR (< 1dB).

Declaration of Competing Interest

The authors declare that they have no known competing financial interests or personal relationships that could have appeared to influence the work reported in this paper.

Acknowledgements

The work was supported by a General Project (No. 51875492) received from the National Natural Science Foundation of China. Z Su acknowledges the support from the Hong Kong Research Grants Council via General Research Funds (Nos. 15202820 and 15204419), and from Hong Kong Innovation and Technology Commission via project “Smart Railway Technology and Applications” (No. K-BBY1). This work was also partially supported by a National Research Foundation of Korea (NRF) grant funded by the Korean government (MSIT) (grant number: 2019R1A3B3067987).

References

[1] Gallot, T., Perge, C., Grenard, V., Fardin, M.-A., Taberlet, N., & Manneville, S. (2013). Ultrafast ultrasonic imaging coupled to rheometry: Principle and illustration. *Review of Scientific Instruments*, *84*(4), 045107.

[2] Yang, X., Wang, K., Zhou, P., Xu, L., Liu, J., Sun, P., & Su, Z. (2022). Ameliorated-multiple signal classification (Am-MUSIC) for damage imaging using a sparse sensor network. *Mechanical Systems and Signal Processing*, *163*, 108154.

[3] Takiy, A. E., Kitano, C., Higuti, R. T., Granja, S. C., Prado, V. T., Elvira, L., & Martínez-Graullera, O. (2017). Ultrasound imaging of immersed plates using high-order Lamb modes at their low attenuation frequency bands. *Mechanical Systems and Signal Processing*, *96*, 321-332.

[4] Huang, Q., & Zeng, Z. (2017). A review on real-time 3D ultrasound imaging technology. *BioMed research international*, *2017*.

[5] Lu, G., Li, Y., Wang, T., Xiao, H., Huo, L., & Song, G. (2017). A multi-delay-and-sum imaging algorithm for damage detection using piezoceramic transducers. *Journal of Intelligent Material Systems and Structures*, *28*(9), 1150-1159.

[6] Zhang, S., Li, X., Jeong, H., & Hu, H. (2018). Experimental investigation of material nonlinearity using the Rayleigh surface waves excited and detected by angle beam wedge transducers. *Ultrasonics*, *89*, 118-125.

[7] Ren, B., & Lissenden, C. J. (2015). PVDF multielement lamb wave sensor for structural health monitoring. *IEEE transactions on ultrasonics, ferroelectrics, and frequency control*, *63*(1), 178-

185.

[8] Cho, H., Hasanian, M., Shan, S., & Lissenden, C. (2019). Nonlinear guided wave technique for localized damage detection in plates with surface-bonded sensors to receive Lamb waves generated by shear-horizontal wave mixing. *NDT and E International*, *102*, 35-46.

[9] Wang, K., Liu, M., Su, Z., Yuan, S., & Fan, Z. (2018). Analytical insight into "breathing" crack-induced acoustic nonlinearity with an application to quantitative evaluation of contact cracks. *Ultrasonics*, *88*, 157-167.

[10] Zhang, Z., Liu, M., Su, Z., & Xiao, Y. (2016). Quantitative evaluation of residual torque of a loose bolt based on wave energy dissipation and vibro-acoustic modulation: A comparative study. *Journal of sound and vibration*, *383*, 156-170.

[11] Hong, M., Mao, Z., Todd, M. D., & Su, Z. (2017). Uncertainty quantification for acoustic nonlinearity parameter in Lamb wave-based prediction of barely visible impact damage in composites. *Mechanical Systems and Signal Processing*, *82*, 448-460.

[12] Su, Y., Xu, L., Zhou, P., Yang, J., Wang, K., Zhou, L.-m., & Su, Z. (2021). Carbon nanotube-decorated glass fibre bundles for cure self-monitoring and load self-sensing of FRPs. *Composites Communications*, 100899.

[13] Zhou, P., Liao, Y., Yang, X., Su, Y., Yang, J., Xu, L., . . . Zhang, Z. (2021). Thermally stable, adhesively strong graphene/polyimide films for inkjet printing ultrasound sensors. *Carbon*, *184*, 64-71.

[14] Liao, Y., Zhou, P., Pan, D., Zhou, L.-m., & Su, Z. (2021). An ultra-thin printable

694 nanocomposite sensor network for structural health monitoring. *Structural Health Monitoring*,
695 *20*(3), 894-903.
696 [15] La Cavera, S., Pérez-Cota, F., Smith, R. J., & Clark, M. (2021). Phonon imaging in 3D with a
697 fibre probe. *Light: Science and Applications*, *10*(1), 1-13.
698 [16] Kumar, A., Gupta, N., Gupta, R., & Kumar, Y. (2005). Effect of coupling conditions on
699 ultrasonic echo parameters. *Journal of Pure and Applied ultrasonics*, *27*(2/3), 70.
700 [17] Gubinyi, Z., Batur, C., Sayir, A., & Dynys, F. (2008). Electrical properties of PZT piezoelectric
701 ceramic at high temperatures. *Journal of Electroceramics*, *20*(2), 95-105.
702 [18] Sony, S., Laventure, S., & Sadhu, A. (2019). A literature review of next‐generation smart
703 sensing technology in structural health monitoring. *Structural Control and Health Monitoring*,
704 *26*(3), e2321.
705 [19] Upadhyay, D., & Schaal, C. (2020). Optimizing the driving trajectories for guided ultrasonic
706 wave excitation using iterative learning control. *Mechanical Systems and Signal Processing*, *144*,
707 106876.
708 [20] Zhong, C. H., Croxford, A. J., & Wilcox, P. D. (2013). Investigation of inductively coupled
709 ultrasonic transducer system for NDE. *IEEE transactions on ultrasonics, ferroelectrics, frequency*
710 *control*, *60*(6), 1115-1125.
711 [21] Jang, J., Liu, P., Kim, B., Kim, S.-w., & Sohn, H. (2020). Silicon wafer crack detection using
712 nonlinear ultrasonic modulation induced by high repetition rate pulse laser. *Optics and Lasers in*
713 *Engineering*, *129*, 106074.

[22] Park, S.-H., Liu, P., Yi, K., Choi, G., Jhang, K.-Y., & Sohn, H. (2021). Mechanical properties estimation of additively manufactured metal components using femtosecond laser ultrasonics and laser polishing. *International Journal of Machine Tools and Manufacture*, *166*, 103745.

[23] Chen, J., Xiao, J., Lisevych, D., & Fan, Z. (2019). Laser-Induced Full-Matrix Ultrasonic Imaging of Complex-Shaped Objects. *IEEE transactions on ultrasonics, ferroelectrics, and frequency control*, *66*(9), 1514-1520.

[24] Li, S., Wang, H., Guo, R., Zhao, J., Zheng, K., Xu, J., . . . Jiang, Y. (2018). Non destructive testing thickness measurement by laser ultrasound under high temperature. *Optik*, *172*, 1140-1154.

[25] Lee, C., & Park, S. (2015). Damage visualization of pipeline structures using laser-induced ultrasonic waves. *Structural Health Monitoring*, *14*(5), 475-488.

[26] Stratoudaki, T., Clark, M., & Wilcox, P. D. (2016). Laser induced ultrasonic phased array using full matrix capture data acquisition and total focusing method. *Optics express*, *24*(19), 21921-21938.

[27] Selim, H., Trull, J., Delgado Prieto, M., Picó, R., Romeral, L., & Cojocaru, C. (2019). Fully Noncontact Hybrid NDT for 3D Defect Reconstruction Using SAFT Algorithm and 2D Apodization Window. *Sensors*, *19*(9), 2138.

[28] Selim, H., Delgado-Prieto, M., Trull, J., Pico, R., Romeral, L., & Cojocaru, C. (2020). Defect reconstruction by non-destructive testing with laser induced ultrasonic detection. *Ultrasonics*, *101*, 106000.

[29] Wu, Z., Chong, S. Y., & Todd, M. D. (2021). Laser ultrasonic imaging of wavefield spatial

734 gradients for damage detection. *Structural Health Monitoring*, *20*(3), 960-977.

735 [30]Ohara, Y., Remillieux, M. C., Onuma, T., Tsunoda, K., Tsuji, T., & Mihara, T. (2020). Toward
736 an ultra-high resolution phased-array system for 3D ultrasonic imaging of solids. *Applied Physics*
737 *Letters*, *117*(11), 111902.

738 [31]Chen, H., Xu, K., Liu, Z., & Ta, D. (2022). Sign coherence factor-based search algorithm for
739 defect localization with laser generated Lamb waves. *Mechanical Systems and Signal Processing*,
740 *173*, 109010.

741 [32]Matsuda, O., Larciprete, M. C., Voti, R. L., & Wright, O. B. (2015). Fundamentals of
742 picosecond laser ultrasonics. *Ultrasonics*, *56*, 3-20.

743 [33]Ruello, P., & Gusev, V. E. (2015). Physical mechanisms of coherent acoustic phonons
744 generation by ultrafast laser action. *Ultrasonics*, *56*, 21-35.

745 [34]Zhang, H., Antoncecchi, A., Edward, S., Setija, I., Planken, P., & Witte, S. (2020). Unraveling
746 phononic, optoacoustic, and mechanical properties of metals with light-driven hypersound.
747 *Physical Review Applied*, *13*(1), 014010.

748 [35]Krylov, V. V. (2016). Directivity patterns of laser-generated sound in solids: Effects of optical
749 and thermal parameters. *Ultrasonics*, *69*, 279-284.

750 [36]Burrows, S. E., Dutton, B., & Dixon, S. (2012). Laser generation of Lamb waves for defect
751 detection: experimental methods and finite element modeling. *IEEE transactions on ultrasonics,*
752 *ferroelectrics, and frequency control*, *59*(1), 82-89.

753 [37]Verrina, V. (2021). *Laser-induced ultrasound for the detection of buried micro-and nano-*

754 *structures* [Doctoral thesis, University of Amsterdam]. Amsterdam.
755 https://ir.arcnl.nl/pub/164/2021-Vanessa-Verrina.pdf
756 [38] Yi, K., Liu, P., Park, S.-H., & Sohn, H. (2022). Femtosecond laser ultrasonic inspection of a
757 moving object and its application to estimation of silicon wafer coating thickness. *Optics and*
758 *Lasers in Engineering*, *148*, 106778.
759 [39] Higuet, J., Valier-Brasier, T., Dehoux, T., & Audoin, B. (2011). Beam distortion detection and
760 deflectometry measurements of gigahertz surface acoustic waves. *Review of Scientific Instruments*,
761 *82*(11), 114905.
762 [40] Jha, A., Azcona, F. J., & Royo, S. (2016). Frequency-modulated optical feedback
763 interferometry for nanometric scale vibrometry. *IEEE Photonics Technology Letters*, *28*(11), 1217-
764 1220.
765 [41] Tachizaki, T., Muroya, T., Matsuda, O., Sugawara, Y., Hurley, D. H., & Wright, O. B. (2006).
766 Scanning ultrafast Sagnac interferometry for imaging two-dimensional surface wave propagation.
767 *Review of Scientific Instruments*, *77*(4), 043713.
768 [42] Zhang, K., & Zhou, Z. (2018). Quantitative characterization of disbonds in multilayered
769 bonded composites using laser ultrasonic guided waves. *NDT and E International*, *97*, 42-50.
770 [43] Liu, P., & Sohn, H. (2016). Numerical simulation of damage detection using laser-generated
771 ultrasound. *Ultrasonics*, *69*, 248-258.
772 [44] Lévesque, D., Dubourg, L., & Blouin, A. (2011). Laser ultrasonics for defect detection and
773 residual stress measurement of friction stir welds. *Nondestructive Testing and Evaluation*, *26*(3-4),

774 319-333.

775 [45]Jiang, Y., Wang, H., Tian, G., Yi, Q., Zhao, J., & Zhen, K. (2019). Fast classification for rail
776 defect depths using a hybrid intelligent method. *Optik*, *180*, 455-468.

777 [46]Boonsang, S., & Dewhurst, R. (2006). A sensitive electromagnetic acoustic transducer for
778 picometer-scale ultrasonic displacement measurements. *Sensors and Actuators A: Physical*, *127*(2),
779 345-354.

780 [47]Blouin, A., Levesque, D., Neron, C., Drolet, D., & Monchalin, J.-P. (1998). Improved
781 resolution and signal-to-noise ratio in laser-ultrasonics by SAFT processing. *Optics express*, *2*(13),
782 531-539.

783 [48]Xu, W., Zhang, J., Li, X., Yuan, S., Ma, G., Xue, Z., . . . Cao, J. (2022). Intelligent denoise
784 laser ultrasonic imaging for inspection of selective laser melting components with rough surface.
785 *NDT and E International*, *125*, 102548.

786 [49]Xue, R., Wang, X., Yang, Q., Dong, F., Zhang, Y., Cao, J., & Song, G. (2019). Grain size
787 characterization of aluminum based on ensemble empirical mode decomposition using a laser
788 ultrasonic technique. *Applied Acoustics*, *156*, 378-386.

789 [50]Ni, C.-Y., Chen, C., Ying, K.-N., Dai, L.-N., Yuan, L., Kan, W.-W., & Shen, Z.-H. (2021).
790 Non-destructive laser-ultrasonic Synthetic Aperture Focusing Technique (SAFT) for 3D
791 visualization of defects. *Photoacoustics*, *22*, 100248.

792 [51]Sadr, A., & Momtaz, A. (2012). Denoising noninvasive laser-ultrasound signals based on
793 combination of wavelet transform and independent component analysis. *Biomedical Engineering:*

794 *Applications, Basis and Communications*, *24*(05), 411-423.

795 [52] Administration, F. A. (2017). Advisory Circular—Damage Tolerance for High Energy Turbine

796 Engine Rotors. In: US Department of Transportation, Washington, DC.

797 [53] Pei, C., Yi, D., Liu, T., Kou, X., & Chen, Z. (2020). Fully noncontact measurement of inner

798 cracks in thick specimen with fiber-phased-array laser ultrasonic technique. *NDT&E International*,

799 102273.

800 [54] Marhenke, T., Neuenschwander, J., Furrer, R., Zolliker, P., Twiefel, J., Hasener, J., . . . Sanabria,

801 S. J. (2020). Air-coupled ultrasound time reversal (ACU-TR) for subwavelength nondestructive

802 imaging. *IEEE transactions on ultrasonics, ferroelectrics, and frequency control*, *67*(3), 651-663.

803 [55] Roux, E., Varray, F., Petrusca, L., Cachard, C., Tortoli, P., & Liebgott, H. (2018). Experimental

804 3-D ultrasound imaging with 2-D sparse arrays using focused and diverging waves. *Scientific*

805 *Reports*, *8*(1), 1-12.

806 [56] Mehdizadeh, S., Austeng, A., Johansen, T. F., & Holm, S. (2012). Eigenspace based minimum

807 variance beamforming applied to ultrasound imaging of acoustically hard tissues. *IEEE*

808 *Transactions on Medical Imaging*, *31*(10), 1912-1921.

809 [57] Diamantis, K., Anderson, T., Butler, M. B., Villagómez-Hoyos, C. A., Jensen, J. A., & Sboros,

810 V. (2019). Resolving ultrasound contrast microbubbles using minimum variance beamforming.

811 *IEEE Transactions on Medical Imaging*, *38*(1), 194-204.

812 [58] Synnevag, J. F., Austeng, A., & Holm, S. (2007). Adaptive beamforming applied to medical

813 ultrasound imaging. *IEEE Transactions on Ultrasonics, Ferroelectric, and Frequency Control*,

54(8), 1606-1613.

[59]Asl, B. M., & Mahloojifar, A. (2011). Contrast enhancement and robustness improvement of adaptive ultrasound imaging using forward-backward minimum variance beamforming. *IEEE transactions on ultrasonics, ferroelectrics, and frequency control*, *58*(4), 858-867.

[60]Zhang, J., & Cheng, Y. (2020). *Despeckling Methods for Medical Ultrasound Images*. Springer.

[61]Zhanabaev, Z. Z., Akhtanov, S., Kozhagulov, E., & Karibayev, B. (2016). Determination of signal-to-noise ratio on the base of information-entropic analysis. *arXiv preprint arXiv:.09212*.

[62]Dai, T., Lu, W., Wang, W., Wang, J., & Xia, S.-T. (2017). Entropy-based bilateral filtering with a new range kernel. *Signal Processing*, *137*, 223-234.

[63]Sternini, S., Pau, A., & Di Scalea, F. L. (2019). Minimum-variance imaging in plates using guided-wave-mode beamforming. *IEEE transactions on ultrasonics, ferroelectrics, and frequency control*, *66*(12), 1906-1919.

[64]Felice, M. V., & Fan, Z. (2018). Sizing of flaws using ultrasonic bulk wave testing: A review. *Ultrasonics*, *88*, 26-42.

[65]Kuperman, W., & Turek, G. (1997). Matched field acoustics. *Mechanical Systems and Signal Processing*, *11*(1), 141-148.

[66]Lorenz, R. G., & Boyd, S. P. (2005). Robust minimum variance beamforming. *IEEE transactions on signal processing*, *53*(5), 1684-1696.

[67]Kaiming, J., Zhigang, W., & Ying, Y. (2012). *Chinese Superalloys Handbook*. Standards Press

834 of China.

835